Electroexcitation of nucleon resonances from CLAS data on single pion electroproduction

I. G. Aznauryan,[1,2] V. D. Burkert,[1] A. S. Biselli,[3] H. Egiyan,[1,4] K. Joo,[5,6] W. Kim,[7] K. Park,[1,7] L. C. Smith,[6] M. Ungaro,[1,5,8] K. P. Adhikari,[9] M. Anghinolfi,[10] H. Avakian,[1] J. Ball,[11] M. Battaglieri,[10] V. Batourine,[1] I. Bedlinskiy,[12] M. Bellis,[13] C. Bookwalter,[14] D. Branford,[23] W. J. Briscoe,[25] W. K. Brooks,[1,39] S. L. Careccia,[9] D. S. Carman,[1] P. L. Cole,[27] P. Collins,[16] V. Crede,[14] A. D'Angelo,[29,35] A. Daniel,[34] R. De Vita,[10] E. De Sanctis,[28] A. Deur,[1] B. Dey,[13] S. Dhamija,[24] R. Dickson,[13] C. Djalali,[37] D. Doughty,[1,21] R. Dupre,[15] A. El Alaoui,[30,*] L. Elouadrhiri,[1] P. Eugenio,[14] G. Fedotov,[36] S. Fegan,[26] T. A. Forest,[9,27] M. Y. Gabrielyan,[24] G. P. Gilfoyle,[22] K. L. Giovanetti,[31] F. X. Girod,[1,11] J. T. Goetz,[17] W. Gohn,[5] E. Golovatch,[36] R. W. Gothe,[37] M. Guidal,[30] L. Guo,[1,†] K. Hafidi,[15] H. Hakobyan,[2,39] C. Hanretty,[14] N. Hassall,[26] D. Heddle,[1,21] K. Hicks,[34] M. Holtrop,[4] C. E. Hyde,[9] Y. Ilieva,[25,37] D. G. Ireland,[26] B. S. Ishkhanov,[36] E. L. Isupov,[36] S. S. Jawalkar,[40] H. S. Jo,[30] J. R. Johnstone,[1,26] D. Keller,[34] M. Khandaker,[33] P. Khetarpal,[8] A. Klein,[9,†] F. J. Klein,[20] L. H. Kramer,[1,24] V. Kubarovsky,[1] S. E. Kuhn,[9] S. V. Kuleshov,[12,39] V. Kuznetsov,[7] K. Livingston,[26] H. Y. Lu,[37] M. Mayer,[9] J. McAndrew,[23] M. E. McCracken,[13] B. McKinnon,[26] C. A. Meyer,[13] T. Mineeva,[5] M. Mirazita,[28] V. Mokeev,[1,36] B. Moreno,[30] K. Moriya,[13] B. Morrison,[16] H. Moutarde,[11] E. Munevar,[25] P. Nadel-Turonski,[20] R. Nasseripour,[24,37,‡] C. S. Nepali,[9] S. Niccolai,[25,30] G. Niculescu,[31] I. Niculescu,[31] M. R. Niroula,[9] M. Osipenko,[10] A. I. Ostrovidov,[14,37] S. Park,[14] E. Pasyuk,[16] S. Anefalos Pereira,[28] S. Pisano,[30] O. Pogorelko,[12] S. Pozdniakov,[12] J. W. Price,[18] S. Procureur,[11] Y. Prok,[6,§] D. Protopopescu,[4,26] B. A. Raue,[1,24] G. Ricco,[10] M. Ripani,[10] B. G. Ritchie,[16] G. Rosner,[26] P. Rossi,[28] F. Sabatié,[11] M. S. Saini,[14] J. Salamanca,[27] R. A. Schumacher,[13] H. Seraydaryan,[9] N. V. Shvedunov,[36] D. I. Sober,[20] D. Sokhan,[23] S. S. Stepanyan,[7] P. Stoler,[8] I. I. Strakovsky,[25] S. Strauch,[25,37] R. Suleiman,[32] M. Taiuti,[10] D. J. Tedeschi,[37] S. Tkachenko,[9] M. F. Vineyard,[38] D. P. Watts,[26,‖] L. B. Weinstein,[9] D. P. Weygand,[1] M. Williams,[13] M. H. Wood,[19] L. Zana,[4] J. Zhang,[9] and B. Zhao[5,¶]

(CLAS Collaboration)

[1]*Thomas Jefferson National Accelerator Facility, Newport News, Virginia 23606, USA*
[2]*Yerevan Physics Institute, 375036 Yerevan, Armenia*
[3]*Fairfield University, Fairfield, Connecticut 06824, USA*
[4]*University of New Hampshire, Durham, New Hampshire 03824-3568, USA*
[5]*University of Connecticut, Storrs, Connecticut 06269, USA*
[6]*University of Virginia, Charlottesville, Virginia 22901, USA*
[7]*Kyungpook National University, Daegu 702-701, Republic of Korea*
[8]*Rensselaer Polytechnic Institute, Troy, New York 12180-3590, USA*
[9]*Old Dominion University, Norfolk, Virginia 23529, USA*
[10]*INFN, Sezione di Genova, I-16146 Genova, Italy*
[11]*CEA, Centre de Saclay, Irfu/Service de Physique Nucléaire, F-91191 Gif-sur-Yvette, France*
[12]*Institute of Theoretical and Experimental Physics, Moscow, RU-117259, Russia*
[13]*Carnegie Mellon University, Pittsburgh, Pennsylvania 15213, USA*
[14]*Florida State University, Tallahassee, Florida 32306, USA*
[15]*Argonne National Laboratory, Argonne, Illinois 60441, USA*
[16]*Arizona State University, Tempe, Arizona 85287-1504, USA*
[17]*University of California at Los Angeles, Los Angeles, California 90095-1547, USA*
[18]*California State University, Dominguez Hills, Carson, California 90747, USA*
[19]*Canisius College, Buffalo, New York, USA*
[20]*Catholic University of America, Washington, DC 20064, USA*
[21]*Christopher Newport University, Newport News, Virginia 23606, USA*
[22]*University of Richmond, Richmond, Virginia 23173, USA*
[23]*Edinburgh University, Edinburgh EH9 3JZ, United Kingdom*
[24]*Florida International University, Miami, Florida 33199, USA*
[25]*The George Washington University, Washington, DC 20052, USA*
[26]*University of Glasgow, Glasgow G12 8QQ, United Kingdom*
[27]*Idaho State University, Pocatello, Idaho 83209, USA*
[28]*INFN, Laboratori Nazionali di Frascati, I-00044 Frascati, Italy*
[29]*INFN, Sezione di Roma Tor Vergata, I-00133 Rome, Italy*
[30]*Institut de Physique Nucléaire ORSAY, Orsay, France*
[31]*James Madison University, Harrisonburg, Virginia 22807, USA*
[32]*Massachusetts Institute of Technology, Cambridge, Massachusetts 02139-4307, USA*
[33]*Norfolk State University, Norfolk, Virginia 23504, USA*
[34]*Ohio University, Athens, Ohio 45701, USA*
[35]*Universita' di Roma Tor Vergata, I-00133 Rome Italy*
[36]*Skobeltsyn Nuclear Physics Institute, RU-119899 Moscow, Russia*

[37] *University of South Carolina, Columbia, South Carolina 29208, USA*
[38] *Union College, Schenectady, New York 12308, USA*
[39] *Universidad Técnica Federico Santa María, Casilla 110-V Valparaíso, Chile*
[40] *College of William and Mary, Williamsburg, Virginia 23187-8795, USA*
(Received 17 September 2009; published 10 November 2009)

We present results on the electroexcitation of the low mass resonances $\Delta(1232)P_{33}$, $N(1440)P_{11}$, $N(1520)D_{13}$, and $N(1535)S_{11}$ in a wide range of Q^2. The results were obtained in the comprehensive analysis of data from the Continuous Electron Beam Accelerator Facility (CEBAF) large acceptance spectrometer (CLAS) detector at the Thomas Jefferson National Accelerator Facility (JLab) on differential cross sections, longitudinally polarized beam asymmetries, and longitudinal target and beam-target asymmetries for π electroproduction off the proton. The data were analyzed using two conceptually different approaches—fixed-t dispersion relations and a unitary isobar model—allowing us to draw conclusions on the model sensitivity of the obtained electrocoupling amplitudes. The amplitudes for the $\Delta(1232)P_{33}$ show the importance of a meson-cloud contribution to quantitatively explain the magnetic dipole strength, as well as the electric and scalar quadrupole transitions. They do not show any tendency of approaching the pQCD regime for $Q^2 \leqslant 6$ GeV^2. For the Roper resonance, $N(1440)P_{11}$, the data provide strong evidence that this state is a predominantly radial excitation of a three-quark ($3q$) ground state. Measured in pion electroproduction, the transverse helicity amplitude for the $N(1535)S_{11}$ allowed us to obtain the branching ratios of this state to the πN and ηN channels via comparison with the results extracted from η electroproduction. The extensive CLAS data also enabled the extraction of the $\gamma^* p \to N(1520)D_{13}$ and $N(1535)S_{11}$ longitudinal helicity amplitudes with good precision. For the $N(1535)S_{11}$, these results became a challenge for quark models and may be indicative of large meson-cloud contributions or of representations of this state that differ from a $3q$ excitation. The transverse amplitudes for the $N(1520)D_{13}$ clearly show the rapid changeover from helicity-3/2 dominance at the real photon point to helicity-1/2 dominance at $Q^2 > 1$ GeV^2, confirming a long-standing prediction of the constituent quark model.

DOI: 10.1103/PhysRevC.80.055203 PACS number(s): 11.55.Fv, 13.40.Gp, 13.60.Le, 14.20.Gk

I. INTRODUCTION

The excitation of nucleon resonances in electromagnetic interactions has long been recognized as an important source of information for understanding the strong interaction in the domain of quark confinement. The Continuous Electron Beam Accelerator Facility (CEBAF) large acceptance spectrometer (CLAS) detector at the Thomas Jefferson National Accelerator Facility (JLab) is the first large acceptance instrument designed for the comprehensive investigation of exclusive electroproduction of mesons with the goal of studying the electroexcitation of nucleon resonances in detail. In recent years, a variety of measurements of single pion electroproduction on protons, including polarization measurements, have been performed at CLAS in a wide range of photon virtuality Q^2 from 0.16 to 6 GeV^2 [1–8]. In this work, we present the results on the electroexcitation of the resonances $\Delta(1232)P_{33}$, $N(1440)P_{11}$, $N(1520)D_{13}$, and $N(1535)S_{11}$, obtained from the comprehensive analysis of these data.

Theoretical and experimental investigations of the electroexcitation of nucleon resonances have a long history, and along with the hadron masses and nucleon electromagnetic characteristics, the information on the $\gamma^* N \to N^*$ transitions played an important role in the justification of the quark model. However, the picture of the nucleon and its excited states, which at first seemed quite simple and was identified as a model of nonrelativistic constituent quarks, turned out to be more complex. One of the reasons for this was the realization that quarks are relativistic objects. A consistent way to perform the relativistic treatment of the $\gamma^* N \to N(N^*)$ transitions is to consider them in the light-front (LF) dynamics [9–11]. The relevant approaches were developed and used to describe the nucleon and its excited states [12–19]. However, much more effort is required to obtain a better understanding of what are the N and N^* LF wave functions and what is their connection to the interquark forces and to the QCD confining mechanism. Another reason is connected with the realization that the traditional picture of baryons built from three constituent quarks is an oversimplified approximation. In the case of the $N(1440)P_{11}$ and $N(1535)S_{11}$, the mass ordering of these states, the large total width of $N(1440)P_{11}$, and the substantial coupling of $N(1535)S_{11}$ to the ηN channel [20] and to strange particles [21,22] are indicative of possible additional $q\bar{q}$ components in the wave functions of these states [23,24] and/or of alternative descriptions. Within dynamical reaction models [25–28], the meson-cloud contribution is identified as a source of the long-standing discrepancy between the data and

*Current address: LPSC-Grenoble, France.
†Current address: Los Alamos National Laboratory, New Mexico, USA.
‡Current address: The George Washington University, Washington, DC 20052, USA.
§Current address: Christopher Newport University, Newport News, Virginia 23606, USA.
‖Current address: Edinburgh University, Edinburgh EH9 3JZ, United Kingdom.
¶Current address: College of William and Mary, Williamsburg, Virginia 23187-8795, USA.

constituent quark model predictions for the $\gamma^*N \to \Delta(1232)P_{33}$ magnetic-dipole amplitude. The importance of pion (cloud) contributions to the transition form factors has also been confirmed by the lattice calculations [29]. Alternative descriptions include the representation of $N(1440)P_{11}$ as a gluonic baryon excitation [30,31] and the possibility that nucleon resonances are meson-baryon molecules generated in chiral coupled-channel dynamics [32–36]. Relations between baryon electromagnetic form factors and generalized parton distributions (GPDs) have also been formulated that connect these two different notions to describe the baryon structure [37,38].

The improvement in accuracy and reliability of the information on the electroexcitation of the nucleon's excited states over a large range in photon virtuality Q^2 is very important for making progress in understanding this complex picture of the strong interaction in the domain of quark confinement.

Our goal is to determine in detail the Q^2 behavior of the electroexcitation of resonances. For this reason, we analyze the data at each Q^2 point separately without imposing any constraints on the Q^2 dependence of the electroexcitation amplitudes. This is in contrast to the analyses by MAID, for instance, MAID2007 [39], where the electroexcitation amplitudes are in part constrained by using parametrizations for their Q^2 dependence.

The analysis was performed using two approaches: fixed-t dispersion relations (DR) and the unitary isobar model (UIM). The real parts of the amplitudes, which contain a significant part of the nonresonant contributions, are built into these approaches in conceptually different ways. This allows us to draw conclusions on the model sensitivity of the resulting electroexcitation amplitudes.

The paper is organized as follows. In Sec. II, we present the data and discuss the stages of the analysis. The approaches we use to analyze the data, DR and UIM, were successfully employed in analyses of pion photoproduction and low-Q^2 electroproduction data, see Refs. [40–42]. In Sec. III, we therefore discuss only the points that need different treatment when we move from low Q^2 to high Q^2. Uncertainties of the background contributions related to the pion and nucleon elastic form factors, and to the $\rho, \omega \to \pi\gamma$ transition form factors are discussed in Sec. IV. In Sec. V, we present how resonance contributions are taken into account and explain how the uncertainties associated with higher resonances and with the uncertainties of masses and widths of the $N(1440)P_{11}$, $N(1520)D_{13}$, and $N(1535)S_{11}$ are accounted for. All these uncertainties are included in the total model uncertainty of the final results. So, in addition to the uncertainties in the data, we have accounted for, as much as possible, the model uncertainties of the extracted $\gamma^*N \to \Delta(1232)P_{33}$, $N(1440)P_{11}$, $N(1520)D_{13}$, and $N(1535)S_{11}$ amplitudes. The results are presented in Sec. VI, compared with model predictions in Sec. VII, and summarized in Sec. VIII.

II. DATA ANALYSIS CONSIDERATIONS

The data are presented in Tables I– IV. They cover the first, second, and part of the third resonance regions. The stages of our analysis are dictated by how we evaluate the influence of higher resonances on the extracted amplitudes for the $\Delta(1232)P_{33}$ and for the resonances from the second resonance region.

TABLE I. Data sets included in the first stage of the analysis, as discussed in the text. The columns corresponding to DR and UIM show the results for χ^2 per data point obtained, respectively, using fixed-t dispersions relations and the unitary isobar model described in Sec. III.

Observable	Q^2 (GeV^2)	W (GeV)	Number of data points (N)	χ^2/N		Ref.
				DR	UIM	
$\frac{d\sigma}{d\Omega}(\pi^+)$	0.3	1.1–1.55	2364	2.06	1.93	[4]
$A_t(\pi^0)$	0.252	1.125–1.55	594	1.36	1.48	[8]
$A_{et}(\pi^0)$	0.252	1.125–1.55	598	1.19	1.23	[8]
$\frac{d\sigma}{d\Omega}(\pi^0)$	0.4	1.1–1.68	3530	1.23	1.24	[1]
$\frac{d\sigma}{d\Omega}(\pi^+)$	0.4	1.1–1.55	2308	1.92	1.64	[4]
$A_{LT'}(\pi^0)$	0.4	1.1–1.66	956	1.24	1.18	[2]
$A_{LT'}(\pi^+)$	0.4	1.1–1.66	918	1.28	1.19	[3]
$A_t(\pi^0)$	0.385	1.125–1.55	696	1.40	1.61	[8]
$A_{et}(\pi^0)$	0.385	1.125–1.55	692	1.22	1.25	[8]
$\frac{d\sigma}{d\Omega}(\pi^0)$	0.525	1.1–1.66	3377	1.33	1.35	[1]
$\frac{d\sigma}{d\Omega}(\pi^+)$	0.5	1.1–1.51	2158	1.51	1.48	[4]
$\frac{d\sigma}{d\Omega}(\pi^0)$	0.65	1.1–1.68	6149	1.09	1.14	[1]
$\frac{d\sigma}{d\Omega}(\pi^+)$	0.6	1.1–1.41	1484	1.21	1.24	[4]
$\frac{d\sigma}{d\Omega}(\pi^+)$	$\simeq 0.6$	1.4–1.76	477	1.72	1.74	[43]
$A_{LT'}(\pi^0)$	0.65	1.1–1.66	805	1.09	1.13	[2]
$A_{LT'}(\pi^+)$	0.65	1.1–1.66	812	1.09	1.04	[3]
$A_t(\pi^0)$	0.611	1.125–1.55	930	1.38	1.40	[8]
$A_{et}(\pi^0)$	0.611	1.125–1.55	923	1.26	1.28	[8]

In the first stage, we analyze the data reported in Table I ($Q^2 = 0.3$–0.65 GeV^2), for which the richest set of polarization measurements is available. The results based on the analysis of the cross sections and longitudinally polarized beam asymmetries ($A_{LT'}$) at $Q^2 = 0.4$ and 0.6–0.65 GeV^2 were already presented in Refs. [41,42]. However, recently, new data have become available from the JLab-CLAS measurements of longitudinal-target (A_t) and beam-target (A_{et}) asymmetries for $\vec{e}\vec{p} \to ep\pi^0$ at $Q^2 = 0.252$, 0.385, and 0.611 GeV^2 [8]. For this reason, we performed a new analysis on the same data set, including these new measurements. We also extended our analysis to the available data for the close values of $Q^2 = 0.3$ and 0.5–0.525 GeV^2. As the asymmetries $A_{LT'}$, A_t, and A_{et} have relatively weak Q^2 dependences, the data on asymmetries at nearby Q^2 were also included in the corresponding sets at $Q^2 = 0.3$ and 0.5–0.525 GeV^2. Following our previous analyses [41,42], we have complemented the data set at $Q^2 =$ 0.6–0.65 GeV^2 with the DESY π^+ cross sections data [43], since the corresponding CLAS data extend over a restricted range in W.

In Ref. [42], the analysis of data at $Q^2 = 0.6$–0.65 GeV^2 was performed in combination with JLab-CLAS data for double-pion electroproduction off the proton [44]. This

TABLE II. $\vec{e}p \to en\pi^+$ data from Ref. [7].

Observable	Q^2 (GeV^2)	W (GeV)	Number of data points (N)	χ^2/N DR	χ^2/N UIM
$\frac{d\sigma}{d\Omega}(\pi^+)$	1.72	1.11–1.69	3530	2.3	2.5
	2.05	1.11–1.69	5123	2.3	2.2
	2.44	1.11–1.69	5452	2.0	2.0
	2.91	1.11–1.69	5484	1.9	2.1
	3.48	1.11–1.69	5482	1.3	1.4
	4.16	1.11–1.69	5778	1.1	1.1
$A_{LT'}(\pi^+)$	1.72	1.12–1.68	699	2.9	3.0
	2.05	1.12–1.68	721	3.0	2.9
	2.44	1.12–1.68	725	3.0	3.0
	2.91	1.12–1.68	767	2.7	2.7
	3.48	1.12–1.68	623	2.4	2.3

allowed us to get information on the electroexcitation amplitudes for the resonances from the third resonance region. This information, combined with the $\gamma p \to N^*$ amplitudes known from photoproduction data [20], sets the ranges of the higher resonance contributions when we extract the amplitudes of the $\gamma^* p \to \Delta(1232)P_{33}$, $N(1440)P_{11}$, $N(1520)D_{13}$, and $N(1535)S_{11}$ transitions from the data reported in Table I.

In the next step, we analyze the data from Table II, which present a large body of $\vec{e}p \to en\pi^+$ differential cross sections and longitudinally polarized electron beam asymmetries at large $Q^2 = 1.72$–4.16 GeV^2 [7]. As the isospin $\frac{1}{2}$ nucleon resonances couple more strongly to the $\pi^+ n$ channel, these data provide large sensitivity to the electrocouplings of the $N(1440)P_{11}$, $N(1520)D_{13}$, and $N(1535)S_{11}$ states. Until recently, the information on the electroexcitation of these resonances at $Q^2 > 1$ GeV^2 was based almost exclusively on the (unpublished) DESY data [45] on $ep \to ep\pi^0$ ($Q^2 \approx 2$ and 3 GeV^2) which have very limited angular coverage. Furthermore, the $\pi^0 p$ final state is coupled more weakly to the isospin $\frac{1}{2}$ states and is dominated by the nearby isospin $\frac{3}{2}$ $\Delta(1232)P_{33}$ resonance. For the $N(1535)S_{11}$, which has a large branching ratio to the ηN channel, there is also information on the $\gamma^* N \to N(1535)S_{11}$ transverse helicity amplitude found from the data on η electroproduction off the proton [46–48].

TABLE III. Low-Q^2 data from Ref. [6] analyzed in the third stage of the analysis.

Observable	Q^2 (GeV^2)	W (GeV)	Number of data points (N)	χ^2/N DR	χ^2/N UIM
$\frac{d\sigma}{d\Omega}(\pi^0)$	0.16	1.1–1.38	3301	1.96	1.98
$\frac{d\sigma}{d\Omega}(\pi^+)$	0.16	1.1–1.38	2909	1.69	1.67
$\frac{d\sigma}{d\Omega}(\pi^0)$	0.20	1.1–1.38	3292	2.29	2.24
$\frac{d\sigma}{d\Omega}(\pi^+)$	0.20	1.1–1.38	2939	1.76	1.78
$\frac{d\sigma}{d\Omega}(\pi^0)$	0.24	1.1–1.38	3086	1.86	1.82
$\frac{d\sigma}{d\Omega}(\pi^+)$	0.24	1.1–1.38	2951	1.49	1.46
$\frac{d\sigma}{d\Omega}(\pi^0)$	0.28	1.1–1.38	2876	1.56	1.59
$\frac{d\sigma}{d\Omega}(\pi^+)$	0.28	1.1–1.38	2941	1.47	1.44
$\frac{d\sigma}{d\Omega}(\pi^0)$	0.32	1.1–1.38	2836	1.51	1.48
$\frac{d\sigma}{d\Omega}(\pi^+)$	0.32	1.1–1.38	2922	1.39	1.37
$\frac{d\sigma}{d\Omega}(\pi^0)$	0.36	1.1–1.38	2576	1.46	1.42
$\frac{d\sigma}{d\Omega}(\pi^+)$	0.36	1.1–1.38	2611	1.35	1.38

TABLE IV. Data included in the third stage of the analysis: the data for $\frac{d\sigma}{d\Omega}(\pi^0)$ at $Q^2 = 0.75$–1.45 and 3–6 GeV^2 are from Refs. [1] and [7], respectively; the data for $\frac{d\sigma}{d\Omega}(\pi^+)$ are from Ref. [43].

Observable	Q^2 (GeV^2)	W (GeV)	Number of data points (N)	χ^2/N DR	χ^2/N UIM
$\frac{d\sigma}{d\Omega}(\pi^0)$	0.75	1.1–1.68	3555	1.16	1.18
$\frac{d\sigma}{d\Omega}(\pi^0)$	0.9	1.1–1.68	3378	1.22	1.25
$\frac{d\sigma}{d\Omega}(\pi^+)$	$\simeq$0.95	1.36–1.76	725	1.62	1.66
$\frac{d\sigma}{d\Omega}(\pi^0)$	1.15	1.1–1.68	1796	1.09	1.15
	1.45	1.1–1.62	1878	1.15	1.18
	3	1.11–1.39	1800	1.41	1.37
	3.5	1.11–1.39	1800	1.22	1.24
	4.2	1.11–1.39	1800	1.16	1.19
	5	1.11–1.39	1800	0.82	0.88
	6	1.11–1.39	1800	0.66	0.67

In the range of Q^2 covered by the data [7] (Table II), there is no information on the helicity amplitudes for the resonances from the third resonance region. The data [7] cover only part of this region and do not allow us to extract reliably the corresponding amplitudes (except those for $N(1680)F_{15}$). For the $\gamma^* p \to N(1440)P_{11}$, $N(1520)D_{13}$, and $N(1535)S_{11}$ amplitudes extracted from the data [7], the evaluation of the uncertainties caused by the lack of information on the resonances from the third resonance region is described in Sec. V.

Finally, we extract the $\gamma^* p \to \Delta(1232)P_{33}$ amplitudes from the data reported in Tables III and IV. These are low-Q^2 data for π^0 and π^+ electroproduction differential cross sections [6] and data for π^0 electroproduction differential cross sections at $Q^2 = 1.15$ and 1.45 GeV^2 [1] and 3–6 GeV^2 [5]. In the analysis of these data, the influence of higher resonances on the results for the $\Delta(1232)P_{33}$ was evaluated by employing the spread of the $\gamma^* p \to N(1440)P_{11}$, $N(1520)D_{13}$, and $N(1535)S_{11}$ amplitudes obtained in the previous stages of our analysis of the data from Tables I and II.

Although the data for $Q^2 = 0.75$–1.45 GeV^2 (Table IV) cover a wide range in W, the absence of π^+ electroproduction data for these Q^2, except $Q^2 = 0.9$ GeV^2, does not allow us to extract the amplitudes for the $N(1440)P_{11}$, $N(1520)D_{13}$, and $N(1535)S_{11}$ resonances with model uncertainties comparable to those for the amplitudes found from the data of Tables I and II. For $Q^2 \simeq 0.95$ GeV^2, there are DESY π^+ electroproduction data [43], which cover the second and third resonance regions, allowing us to extract amplitudes for all resonances from the first and second resonance regions at $Q^2 = 0.9$–0.95 GeV^2. To evaluate the uncertainties caused

by the higher mass resonances, we have used for $Q^2 = 0.9$–0.95 GeV^2 the same procedure as for the data from Table II.

III. ANALYSIS APPROACHES

The approaches we use to analyze the data—DR and UIM—are described in detail in Refs. [40,41] and were successfully employed in Refs. [40–42] for the analyses of pion-photoproduction and low-Q^2 electroproduction data. In this section, we discuss certain aspects of these approaches that need a different treatment as we move to higher Q^2.

A. Dispersion relations

We use fixed-t dispersion relations for invariant amplitudes defined in accordance with the following definition of the electromagnetic current I^μ for the $\gamma^* N \to \pi N$ process [49]:

$$I^\mu \equiv \bar{u}(p_2)\gamma_5 \mathcal{I}^\mu u(p_1)\phi_\pi, \tag{1}$$

$$\mathcal{I}^\mu = \frac{B_1}{2}[\gamma^\mu \not{k} - \not{k}\gamma^\mu] + 2P^\mu B_2 + 2q^\mu B_3 + 2k^\mu B_4 - \gamma^\mu B_5 + \not{k}P^\mu B_6 + \not{k}k^\mu B_7 + \not{k}q^\mu B_8, \tag{2}$$

where k, q, p_1, p_2 are the four-momenta of the virtual photon, pion, and initial and final nucleons, respectively; $P = \frac{1}{2}(p_1 + p_2)$, $B_1(s,t,Q^2)$, $B_2(s,t,Q^2)$, $\ldots$, $B_8(s,t,Q^2)$ are the invariant amplitudes that are functions of the invariant variables $s = (k+p_1)^2$, $t = (k-q)^2$, and $Q^2 \equiv -k^2$; $u(p_1)$ and $u(p_2)$ are the Dirac spinors of the initial and final state nucleons, and ϕ_π is the pion field.

The conservation of I^μ leads to the relations

$$4Q^2 B_4 = (s-u)B_2 - 2\big(t + Q^2 - m_\pi^2\big)B_3, \tag{3}$$

$$2Q^2 B_7 = -2B_5' - \big(t + Q^2 - m_\pi^2\big)B_8, \tag{4}$$

where $B_5' \equiv B_5 - \frac{1}{4}(s-u)B_6$. Therefore, only six of the eight invariant amplitudes are independent. In Ref. [40], the following independent amplitudes were chosen: B_1, B_2, B_3, B_5', B_6, B_8. Taking into account the isotopic structure, we have 18 independent invariant amplitudes. For the amplitudes $B_1^{(\pm,0)}$, $B_2^{(\pm,0)}$, $B_3^{(+,0)}$, $B'^{(\pm,0)}_5$, $B_6^{(\pm,0)}$, and $B_8^{(\pm,0)}$, unsubtracted dispersion relations at fixed t can be written. The only exception is the amplitude $B_3^{(-)}$, for which a subtraction is necessary:

$$\mathrm{Re}B_3^{(-)}(s,t,Q^2) = f_{\rm sub}(t,Q^2) - ge\frac{F_\pi(Q^2)}{t-m_\pi^2} - \frac{ge}{4}\big[F_1^p(Q^2) - F_1^n(Q^2)\big] \times \left(\frac{1}{s-m^2} + \frac{1}{u-m^2}\right) + \frac{P}{\pi}\int_{s_{\rm thr}}^{\infty} \mathrm{Im}B_3^{(-)}(s',t,Q^2) \times \left(\frac{1}{s'-s} + \frac{1}{s'-u}\right) ds', \tag{5}$$

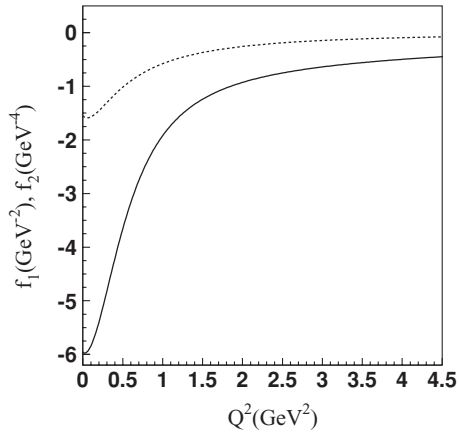

FIG. 1. Q^2 dependence of the coefficients $f_1(Q^2)$ (solid curve) and $f_2(Q^2)$ (dashed curve) from Eq. (7). The results for $Q^2 < 0.7$ GeV^2 were found using Eq. (6), whereas the results for $Q^2 = 1.7$–4.5 GeV^2 are from the fit to the data [7].

where $g^2/4\pi = 13.8$, $e^2/4\pi = 1/137$, $F_\pi(Q^2)$ is the pion form factor, $F_1^N(Q^2)$ is the nucleon Pauli form factor, and m and m_π are the nucleon and pion masses, respectively.

At $Q^2 = 0$, using the relation $B_3 = B_2 \frac{s-u}{2(t-m_\pi^2)}$, which follows from Eq. (3), and DR for the amplitude $B_2(s,t,Q^2=0)$, one obtains

$$f_{\rm sub}(t,Q^2) = 4\frac{P}{\pi}\int_{s_{\rm thr}}^{\infty} \frac{\mathrm{Im}B_3^{(-)}(s',t,Q^2)}{u'-s'}ds', \tag{6}$$

where $u' = 2m^2 + m_\pi^2 - Q^2 - s' - t$.

This expression for $f_{\rm sub}(t,Q^2)$ was successfully used for the analysis of pion-photoproduction and low-Q^2 (0.4, 0.65 GeV^2) electroproduction data [40,41]. However, it turned out that it is not suitable at higher Q^2. Using a simple parametrization,

$$f_{\rm sub}(t,Q^2) = f_1(Q^2) + f_2(Q^2)t, \tag{7}$$

a suitable subtraction was found from the fit to the data for $Q^2 = 1.7$–4.5 GeV^2 [7]. The linear parametrization in t is also consistent with the subtraction found from Eq. (6) at low Q^2. Figure 1 demonstrates a smooth transition of the results for the coefficients $f_1(Q^2)$, $f_2(Q^2)$ found at low Q^2 (<0.7 GeV^2) using Eq. (6) to those at large Q^2 (1.7–4.5 GeV^2) found from the fit to the data [7].

Figure 2 shows the relative contribution of $f_{\rm sub}(t,Q^2)$ compared with the pion contribution in Eq. (5) at $Q^2 = 0$ and $Q^2 = 2.44$ GeV^2. It can be seen that the contribution of $f_{\rm sub}(t,Q^2)$ is comparable with the pion contribution only at large $|t|$, where the latter is small. At small $|t|$, $f_{\rm sub}(t,Q^2)$ is very small compared to the pion contribution.

B. Unitary isobar model

The UIM of Ref. [40] was developed on the basis of the model of Ref. [50]. One of the modifications made in Ref. [40] involved the incorporation of Regge poles with increasing energies. This allowed us to describe pion photoproduction multipole amplitudes [51,52] with a unified Breit-Wigner

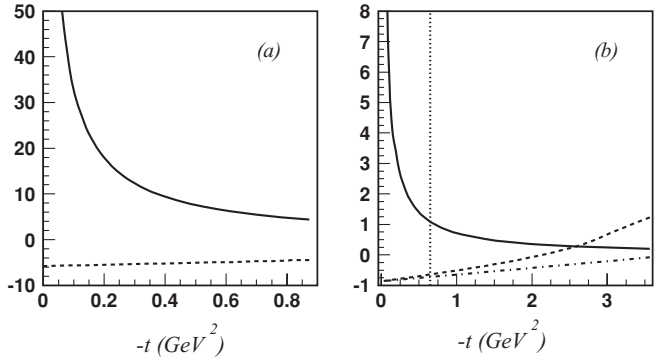

FIG. 2. Pion contribution in GeV^{-2} units (solid curves) to the DR for the amplitude $B_3^{(-)}(s,t,Q^2)$, Eq. (5), compared with $f_{\rm sub}(t,Q^2)$ at (a) $Q^2=0$ and (b) $Q^2=2.44$ GeV^2. The dashed curves represent $f_{\rm sub}(t,Q^2)$ taken in the form of Eq. (6); the dash-dotted curve corresponds to the results for $f_{\rm sub}(t,Q^2)$ obtained by fitting the data [7]. At $Q^2=2.44$ GeV^2, the physical region is located on the right side of the dotted vertical line.

parametrization of resonance contributions in the form close to that introduced by Walker [53]. The Regge-pole amplitudes were constructed using a gauge invariant Regge-trajectory-exchange model developed in Refs. [54,55]. This model gives a good description of the pion photoproduction data above the resonance region and can be extended to finite Q^2 [56].

The incorporation of Regge poles into the background of UIM, built from the nucleon exchanges in the s and u channels and the t-channel π, ρ, and ω exchanges, was made in Ref. [40] in the following way:

$$\begin{aligned}\text{Background} &= [N+\pi+\rho+\omega]_{\rm UIM} \quad \text{at} \quad s<s_0,\\ &= [N+\pi+\rho+\omega]_{\rm UIM}\frac{1}{1+(s-s_0)^2}\\ &\quad +\text{Re}[\pi+\rho+\omega+b_1+a_2]_{\rm Regge}\\ &\quad \times\frac{(s-s_0)^2}{1+(s-s_0)^2} \quad \text{at} \quad s>s_0. \end{aligned} \tag{8}$$

Here the Regge-pole amplitudes were taken from Refs. [54,55] and consisted of Reggeized π,ρ,ω,b_1, and a_2 t-channel exchange contributions. This background was unitarized in the K-matrix approximation. The value of $s_0\simeq 1.2$ GeV^2 was found in Ref. [40] from the description of the pion photoproduction multipole amplitudes [51,52]. With this value of s_0, we obtained a good description of π electroproduction data at $Q^2=0.4$ and 0.65 GeV^2 in the first, second, and third resonance regions [41,42]. The modification of Eq. (8) was important in obtaining a better description of the data in the second and third resonance regions, but it played an insignificant role at $\sqrt{s}<1.4$ GeV.

When the relation in Eq. (8) was applied for $Q^2\geqslant 0.9$ GeV^2, the best description of the data was obtained with $\sqrt{s_0}>1.8$ GeV. Consequently, in the analysis of the data [7], the background of UIM was built just from the nucleon exchanges in the s and u channels and the t-channel π, ρ, and ω exchanges.

IV. N,π,ρ,ω CONTRIBUTIONS

In both the DR and UIM approaches, the nonresonant background contains Born terms corresponding to the s- and u-channel nucleon exchanges and t-channel pion contribution and therefore depends on the proton, neutron, and pion form factors. The background of the UIM also contains the ρ and ω t-channel exchanges and, therefore, the contribution of the form factors $G_{\rho(\omega)\to\pi\gamma}(Q^2)$. All these form factors, except the neutron electric and $G_{\rho(\omega)\to\pi\gamma}(Q^2)$ ones, are known in the region of Q^2 that is the subject of this study. For the proton form factors, we used the parametrizations found for the existing data in Ref. [57]. The neutron magnetic form factor and the pion form factor were taken from Refs. [58,59] and [60–63], respectively. The neutron electric form factor $G_{E_n}(Q^2)$ is measured up to $Q^2=1.45$ GeV^2 [64], and Ref. [64] presents a parametrization for all existing data on $G_{E_n}(Q^2)$, which we used for the extrapolation of $G_{E_n}(Q^2)$ to $Q^2>1.45$ GeV^2. In our final results at high Q^2, we allow for up to a 50% deviation from this parametrization, which is accounted for in the systematic uncertainty. There are no measurements of the form factors $G_{\rho(\omega)\to\pi\gamma}(Q^2)$; however, investigations made using both QCD sum rules [65] and a quark model [66] predict a Q^2 dependence of $G_{\rho(\omega)\to\pi\gamma}(Q^2)$ close to the dipole form $G_D(Q^2)=1/(1+\frac{Q^2}{0.71\ \text{GeV}^2})^2$. We used this dipole form in our analysis and introduced in our final results a systematic uncertainty that accounts for a 20% deviation from 0.71 GeV^2. All uncertainties, including those arising from the measured proton, neutron, and pion form factors, were added in quadrature and will be, as one part of our total model uncertainties, referenced as model uncertainties (I) of our results.

V. RESONANCE CONTRIBUTIONS

We have taken into account all well-established resonances from the first, second, and third resonance regions. These are four- and three-star resonances: $\Delta(1232)P_{33}$, $N(1440)P_{11}$, $N(1520)D_{13}$, $N(1535)S_{11}$, $\Delta(1600)P_{33}$, $\Delta(1620)S_{31}$, $N(1650)S_{11}$, $N(1675)D_{15}$, $N(1680)F_{15}$, $N(1700)D_{13}$, $\Delta(1700)D_{33}$, $N(1710)P_{11}$, and $N(1720)P_{13}$. For the masses, widths, and πN branching ratios of these resonances, we used the mean values of the data from the Review of Particle Physics (RPP) [20]. They are presented in Table V. Resonances of the fourth resonance region have no influence in the energy region under investigation and were not included.

Resonance contributions to the multipole amplitudes were parametrized in the usual Breit-Wigner form with energy-dependent widths [53]. An exception was made for the $\Delta(1232)P_{33}$ resonance, which was treated differently. According to the phase-shift analyses of πN scattering, the πN amplitude corresponding to the $\Delta(1232)P_{33}$ resonance is elastic up to $W=1.43$ GeV (see, for example, the latest George Washington University (GWU) analyses [67,68]). In combination with DR and Watson's theorem, this provides strict constraints on the multipole amplitudes $M_{1+}^{3/2}$, $E_{1+}^{3/2}$, and $S_{1+}^{3/2}$ that correspond to the $\Delta(1232)P_{33}$ resonance [40]. In particular, it was shown [40] that with increasing Q^2, the

TABLE V. Masses, widths, and branching ratios of the resonances included in our analysis. The quoted ranges are taken from RPP [20]. The quantities labeled by tildes ($\tilde{M}$, $\tilde{\Gamma}$, $\tilde{\beta}_{\pi N}$) correspond to the values used in the analysis and in the extraction of the $\gamma^* p \to N^*$ helicity amplitudes.

N^*	M (MeV)	$\tilde{M}$ (MeV)	Γ (MeV)	$\tilde{\Gamma}$ (MeV)	$\beta_{\pi N}$ (%)	$\tilde{\beta}_{\pi N}$ (%)
$\Delta(1232)P_{33}$	1231–1233	1232	116–120	118	100	100
$N(1440)P_{11}$	1420–1470	1440	200–450	350	55–75	60
$N(1520)D_{13}$	1515–1525	1520	100–125	112	55–65	60
$N(1535)S_{11}$	1525–1545	1535	125–175	150	35–55	45
$\Delta(1600)P_{33}$	1550–1700	1600	250–450	350	10–25	20
$\Delta(1620)S_{31}$	1600–1660	1630	135–150	145	20–30	25
$N(1650)S_{11}$	1645–1670	1655	145–185	165	60–95	75
$N(1675)D_{15}$	1670–1680	1675	130–165	150	35–45	40
$N(1680)F_{15}$	1680–1690	1685	120–140	130	65–70	65
$N(1700)D_{13}$	1650–1750	1700	50–150	100	5–15	10
$\Delta(1700)D_{33}$	1670–1750	1700	200–400	300	10–20	15
$N(1710)P_{11}$	1680–1740	1710	50–250	100	10–20	15
$N(1720)P_{13}$	1700–1750	1720	150–300	200	10–20	15

W dependence of $M_{1+}^{3/2}$ remains unchanged and close to that from the GWU analysis [52] at $Q^2 = 0$, if the same normalizations of the amplitudes at the resonance position are used. This constraint on the large $M_{1+}^{3/2}$ amplitude plays an important role in the reliable extraction of the amplitudes for the $\gamma^* N \to \Delta(1232)P_{33}$ transition. It also impacts the analysis of the second resonance region, because resonances from this region overlap with the $\Delta(1232)P_{33}$.

The fitting parameters in our analyses were the $\gamma^* p \to N^*$ helicity amplitudes $A_{1/2}$, $A_{3/2}$, and $S_{1/2}$. They are related to the resonant portions of the multipole amplitudes at the resonance positions. For the resonances with $J^P = \frac{1}{2}^-, \frac{3}{2}^+, \ldots$, these relations are the following:

$$A_{1/2} = -\frac{1}{2}[(l+2)\mathcal{E}_{l+} + l\mathcal{M}_{l+}], \tag{9}$$

$$A_{3/2} = \frac{[l(l+2)]^{1/2}}{2}(\mathcal{E}_{l+} - \mathcal{M}_{l+}), \tag{10}$$

$$S_{1/2} = -\frac{1}{\sqrt{2}}(l+1)\mathcal{S}_{l+}. \tag{11}$$

For the resonances with $J^P = \frac{1}{2}^+, \frac{3}{2}^-, \ldots$,

$$A_{1/2} = \frac{1}{2}[(l+2)\mathcal{M}_{(l+1)-} - l\mathcal{E}_{(l+1)-}], \tag{12}$$

$$A_{3/2} = -\frac{[l(l+2)]^{1/2}}{2}(\mathcal{E}_{(l+1)-} + \mathcal{M}_{(l+1)-}), \tag{13}$$

$$S_{1/2} = -\frac{1}{\sqrt{2}}(l+1)\mathcal{S}_{(l+1)-}, \tag{14}$$

where J and P are the spin and parity of the resonance, $l = J - \frac{1}{2}$, and

$$\mathcal{M}_{l\pm}(\mathcal{E}_{l\pm}, \mathcal{S}_{l\pm}) \equiv a\mathrm{Im}M_{l\pm}^R\left(E_{l\pm}^R, S_{l\pm}^R\right)\ (W = M),$$
$$a \equiv \frac{1}{C_I}\left[(2J+1)\pi\frac{q_r}{K}\frac{M}{m}\frac{\Gamma}{\beta_{\pi N}}\right]^{1/2},$$

$$C_{1/2} = -\sqrt{\frac{1}{3}}, \quad C_{3/2} = \sqrt{\frac{2}{3}} \quad \text{for } \gamma^* p \to \pi^0 p,$$
$$C_{1/2} = -\sqrt{\frac{2}{3}}, \quad C_{3/2} = -\sqrt{\frac{1}{3}} \quad \text{for } \gamma^* p \to \pi^+ n. \tag{15}$$

Here C_I are the isospin Clebsch-Gordon coefficients in the decay $N^* \to \pi N$; Γ, M, and I are the total width, mass, and isospin of the resonance, respectively, $\beta_{\pi N}$ is its branching ratio to the πN channel, and K and q_r are the photon equivalent energy and the pion momentum at the resonance position in the c.m. system. For the transverse amplitudes $A_{1/2}$ and $A_{3/2}$, these relations were introduced by Walker [53]; for the longitudinal amplitudes, they agree with those from Refs. [15,69,70].

The masses, widths, and πN branching ratios of the resonances are known in the ranges presented in Table V. The uncertainties of masses and widths of the $N(1440)P_{11}$, $N(1520)D_{13}$, and $N(1535)S_{11}$ are quite significant and can affect the resonant portions of the multipole amplitudes for these resonances at the resonance positions. These uncertainties were taken into account by refitting the data multiple times with the width (mass) of each of the resonances changed within one standard deviation[1] while keeping those for other resonances fixed. The resulting uncertainties of the $\gamma^* p \to N(1440)P_{11}$, $N(1520)D_{13}$, $N(1535)S_{11}$ amplitudes were added in quadrature and considered as model uncertainties (II).

In Sec. II, we discussed that in the analysis of the data reported in Table II, there is another uncertainty in the amplitudes for the $N(1440)P_{11}$, $N(1520)D_{13}$, and $N(1535)S_{11}$, which is caused by the limited information available on magnitudes of resonant amplitudes in the third resonance region. To

[1]The standard deviations were defined as $\sigma_M = (M_{\max} - M_{\min})/\sqrt{12}$ and $\sigma_\Gamma = (\Gamma_{\max} - \Gamma_{\min})/\sqrt{12}$, with the maximum and minimum values as shown in Table V.

TABLE VI. Results for the imaginary part of $M_{1+}^{3/2}$ at $W = 1.232$ GeV. For the DR and UIM results, the first and second uncertainties are the statistical uncertainty from the fit and the model uncertainty (I) (see Sec. IV), respectively. For $Q^2 = 0.3$–1.45 GeV^2, uncertainty (I) is practically related only to the form factors $G_{\rho,\omega}(Q^2)$; for this reason it does not affect the amplitudes found using DR. Final results are the average values of the amplitudes found using DR and UIM; here the first uncertainty is statistical, and the second one is the model uncertainty discussed in Sec. VI.

Q^2 (GeV^2)	Im$M_{1+}^{3/2}$ ($\sqrt{\mu}$b), $W = 1.232$ GeV		
	DR	UIM	Final results
0.3	5.173 ± 0.130	$5.122 \pm 0.130 \pm 0.004$	$5.148 \pm 0.130 \pm 0.026$
0.4	4.843 ± 0.122	$4.803 \pm 0.122 \pm 0.005$	$4.823 \pm 0.122 \pm 0.021$
0.525	4.277 ± 0.109	$4.238 \pm 109 \pm 0.008$	$4.257 \pm 0.109 \pm 0.021$
0.65	3.814 ± 0.097	$3.794 \pm 0.097 \pm 0.009$	$3.804 \pm 0.097 \pm 0.013$
0.75	3.395 ± 0.088	$3.356 \pm 0.088 \pm 0.011$	$3.375 \pm 0.088 \pm 0.022$
0.9	3.010 ± 0.078	$2.962 \pm 0.078 \pm 0.012$	$2.986 \pm 0.078 \pm 0.027$
1.15	2.487 ± 0.066	$2.438 \pm 0.066 \pm 0.013$	$2.463 \pm 0.066 \pm 0.028$
1.45	1.948 ± 0.059	$1.880 \pm 0.059 \pm 0.014$	$1.914 \pm 0.059 \pm 0.037$
3.0	$0.725 \pm 0.022 \pm 0.011$	$0.693 \pm 0.022 \pm 0.016$	$0.709 \pm 0.022 \pm 0.023$
3.5	$0.582 \pm 0.018 \pm 0.012$	$0.558 \pm 0.018 \pm 0.017$	$0.570 \pm 0.018 \pm 0.021$
4.2	$0.434 \pm 0.014 \pm 0.014$	$0.412 \pm 0.014 \pm 0.018$	$0.423 \pm 0.014 \pm 0.021$
5.0	$0.323 \pm 0.012 \pm 0.021$	$0.312 \pm 0.012 \pm 0.023$	$0.317 \pm 0.012 \pm 0.024$
6.0	$0.200 \pm 0.012 \pm 0.024$	$0.191 \pm 0.012 \pm 0.027$	$0.196 \pm 0.012 \pm 0.027$

evaluate the influence of these states on the extracted $\gamma^* p \to N(1440)P_{11}$, $N(1520)D_{13}$, and $N(1535)S_{11}$ amplitudes, we used two ways of estimating their strength:

(i) Directly including these states in the fit, taking the corresponding amplitudes $A_{1/2}$, $A_{3/2}$, $S_{1/2}$ as free parameters.

(ii) Applying some constraints on their amplitudes. Using symmetry relations within the $[70, 1^-]$ multiplet given by the single quark transition model [71], we have related the transverse amplitudes for the members of this multiplet [$\Delta(1620)S_{31}$, $N(1650)S_{11}$, $N(1675)D_{15}$, $N(1700)D_{13}$, and $\Delta(1700)D_{33}$] to the amplitudes of $N(1520)D_{13}$ and $N(1535)S_{11}$ that are well determined in the analysis. The longitudinal amplitudes of these resonances and the amplitudes of the resonances $\Delta(1600)P_{33}$ and $N(1710)P_{11}$, which have small photocouplings [20] and are not seen in low-Q^2 π and 2π electroproduction [42], were assumed to be zero.

The results obtained for $N(1440)P_{11}$, $N(1520)D_{13}$, and $N(1535)S_{11}$ using the two procedures are very close to each other. The amplitudes for these resonances presented below are the average values of the results obtained in these fits. The uncertainties arising from this averaging procedure were added in quadrature to the model uncertainties (II).

VI. RESULTS

Results for the extracted $\gamma^* p \to \Delta(1232)P_{33}$, $N(1440)P_{11}$, $N(1520)D_{13}$, and $N(1535)S_{11}$ amplitudes are presented in Tables VI–XII. Here we show separately the amplitudes obtained in the DR and UIM approaches. The amplitudes are presented with the fit errors and model uncertainties caused by the N, π, ρ, and ω contributions to the background and those caused by the masses and widths of the $N(1440)P_{11}$, $N(1520)D_{13}$, and $N(1535)S_{11}$, and by the resonances of the third resonance region. These uncertainties, discussed in Secs. IV and V and referred to as model uncertainties (I) and (II), were added in quadrature and represent model uncertainties of the DR and UIM results.

TABLE VII. Results for the ratio $R_{EM} \equiv \text{Im}E_{1+}^{3/2}/\text{Im}M_{1+}^{3/2}$ at $W = 1.232$ GeV. All other relevant information is as given in the legend of Table VI.

Q^2 (GeV^2)	R_{EM} (%)		
	DR	UIM	Final results
0.16	-2.0 ± 0.1	$-1.7 \pm 0.1 \pm 0.04$	$-1.9 \pm 0.1 \pm 0.2$
0.2	-1.9 ± 0.2	$-1.6 \pm 0.2 \pm 0.04$	$-1.8 \pm 0.2 \pm 0.2$
0.24	-2.2 ± 0.2	$-2.1 \pm 0.2 \pm 0.1$	$-2.2 \pm 0.2 \pm 0.1$
0.28	-1.9 ± 0.2	$-1.6 \pm 0.2 \pm 0.1$	$-1.8 \pm 0.2 \pm 0.2$
0.3	-2.2 ± 0.2	$-2.1 \pm 0.2 \pm 0.1$	$-2.1 \pm 0.2 \pm 0.1$
0.32	-1.9 ± 0.2	$-1.6 \pm 0.2 \pm 0.1$	$-1.8 \pm 0.2 \pm 0.2$
0.36	-1.8 ± 0.2	$-1.5 \pm 0.3 \pm 0.1$	$-1.7 \pm 0.3 \pm 0.2$
0.4	-2.9 ± 0.2	$-2.4 \pm 0.2 \pm 0.1$	$-2.7 \pm 0.2 \pm 0.3$
0.525	-2.3 ± 0.3	$-2.0 \pm 0.3 \pm 0.1$	$-2.2 \pm 0.3 \pm 0.2$
0.65	-2.0 ± 0.4	$-1.4 \pm 0.3 \pm 0.1$	$-1.7 \pm 0.4 \pm 0.3$
0.75	-2.2 ± 0.4	$-1.9 \pm 0.4 \pm 0.1$	$-2.1 \pm 0.4 \pm 0.2$
0.9	-2.4 ± 0.5	$-2.1 \pm 0.5 \pm 0.2$	$-2.2 \pm 0.5 \pm 0.3$
1.15	-2.0 ± 0.6	$-2.6 \pm 0.5 \pm 0.2$	$-2.3 \pm 0.6 \pm 0.4$
1.45	-2.4 ± 0.7	$-2.5 \pm 0.7 \pm 0.2$	$-2.5 \pm 0.7 \pm 0.2$
3.0	$-1.6 \pm 0.4 \pm 0.1$	$-2.3 \pm 0.4 \pm 0.2$	$-2.0 \pm 0.4 \pm 0.4$
3.5	$-1.8 \pm 0.5 \pm 0.2$	$-1.1 \pm 0.5 \pm 0.3$	$-1.5 \pm 0.5 \pm 0.5$
4.2	$-2.3 \pm 0.8 \pm 0.3$	$-2.9 \pm 0.7 \pm 0.4$	$-2.6 \pm 0.8 \pm 0.4$
5.0	$-2.2 \pm 1.4 \pm 0.3$	$-3.2 \pm 1.5 \pm 0.4$	$-2.7 \pm 1.5 \pm 0.6$
6.0	$-2.1 \pm 2.5 \pm 1.1$	$-3.6 \pm 2.6 \pm 1.5$	$-2.8 \pm 2.6 \pm 1.7$

TABLE VIII. Results for the ratio $R_{SM} \equiv \mathrm{Im}S_{1+}^{3/2}/\mathrm{Im}M_{1+}^{3/2}$ at $W = 1.232$ GeV. All other relevant information is as given in the legend of Table VI.

Q^2 (GeV^2)	R_{SM} (%)		
	DR	UIM	Final results
0.16	-4.8 ± 0.2	$-4.6 \pm 0.2 \pm 0.04$	$-4.7 \pm 0.2 \pm 0.1$
0.2	-4.9 ± 0.2	$-4.4 \pm 0.2 \pm 0.1$	$-4.7 \pm 0.2 \pm 0.3$
0.24	-4.7 ± 0.3	$-4.5 \pm 0.3 \pm 0.1$	$-4.6 \pm 0.3 \pm 0.1$
0.28	-5.6 ± 0.3	$-5.4 \pm 0.3 \pm 0.1$	$-5.5 \pm 0.3 \pm 0.1$
0.3	-5.4 ± 0.2	$-5.0 \pm 0.2 \pm 0.1$	$-5.2 \pm 0.2 \pm 0.2$
0.32	-5.9 ± 0.3	$-5.5 \pm 0.3 \pm 0.1$	$-5.7 \pm 0.3 \pm 0.2$
0.36	-5.5 ± 0.3	$-5.2 \pm 0.3 \pm 0.1$	$-5.4 \pm 0.3 \pm 0.2$
0.4	-5.9 ± 0.2	$-5.2 \pm 0.2 \pm 0.1$	$-5.5 \pm 0.2 \pm 0.4$
0.525	-6.0 ± 0.3	$-5.5 \pm 0.3 \pm 0.1$	$-5.8 \pm 0.3 \pm 0.3$
0.65	-7.0 ± 0.4	$-6.2 \pm 0.4 \pm 0.2$	$-6.6 \pm 0.4 \pm 0.4$
0.75	-7.3 ± 0.4	$-6.7 \pm 0.4 \pm 0.2$	$-7.0 \pm 0.4 \pm 0.4$
0.9	-8.6 ± 0.4	$-8.1 \pm 0.4 \pm 0.2$	$-8.4 \pm 0.5 \pm 0.3$
1.15	-8.8 ± 0.5	$-8.0 \pm 0.5 \pm 0.2$	$-8.4 \pm 0.5 \pm 0.4$
1.45	-10.5 ± 0.8	$-9.6 \pm 0.8 \pm 0.2$	$-10.1 \pm 0.8 \pm 0.5$
3.0	$-12.6 \pm 0.6 \pm 0.1$	$-11.4 \pm 0.6 \pm 0.2$	$-12.0 \pm 0.6 \pm 0.6$
3.5	$-12.8 \pm 0.8 \pm 0.3$	$-12.4 \pm 0.8 \pm 0.4$	$-12.6 \pm 0.8 \pm 0.4$
4.2	$-17.1 \pm 1.2 \pm 0.5$	$-15.9 \pm 1.3 \pm 0.7$	$-16.5 \pm 1.3 \pm 0.8$
5.0	$-26.6 \pm 2.7 \pm 1.2$	$-25.2 \pm 2.7 \pm 1.5$	$-25.9 \pm 2.7 \pm 1.7$
6.0	$-26.4 \pm 5.2 \pm 3.2$	$-25.3 \pm 5.3 \pm 3.8$	$-25.9 \pm 5.3 \pm 3.8$

The DR and UIM approaches give comparable descriptions of the data (see χ^2 values in Tables I–IV), and, therefore, the differences in $A_{1/2}$, $A_{3/2}$, and $S_{1/2}$ are related only to the model assumptions. We, therefore, ascribe the difference in the results obtained in the two approaches to model uncertainty, and present as our final results in Tables VI–X and XII the mean values of the amplitudes extracted using DR and UIM. The uncertainty that originates from the averaging is considered as an additional model uncertainty—uncertainty (III). Along with the average values of uncertainties (I) and (II) obtained in the DR and UIM approaches, it is included in quadrature in the total model uncertainties of the average amplitudes.

In the fit, we have included the experimental point-to-point systematics by adding them in quadrature with the statistical error. We also took into account the overall normalization error of the CLAS cross section data, which is about 5%. It was checked that the overall normalization error results in modifications of all extracted amplitudes, except $M_{1+}^{3/2}$, that are significantly smaller than the fit errors of these amplitudes. For $M_{1+}^{3/2}$, this error results in an overall normalization error that is larger than the fit error. It is about 2.5% for low Q^2, and

TABLE IX. Results for the $\gamma^* p \to N(1440)P_{11}$ helicity amplitudes in units of 10^{-3} GeV$^{-1/2}$. For the DR and UIM results, the first and second uncertainties are, respectively, the statistical uncertainty from the fit and the model uncertainty, which consists of uncertainties (I) (Sec. IV) and (II) (Sec. V) added in quadrature. Final results are the average values of the amplitudes found using DR and UIM; here the first uncertainty is statistical and the second one is the model uncertainty discussed in Sec. VI.

Q^2 (GeV^2)	DR		UIM		Final results	
	$A_{1/2}$	$S_{1/2}$	$A_{1/2}$	$S_{1/2}$	$A_{1/2}$	$S_{1/2}$
0.3	$-15.5 \pm 1.2 \pm 1.0$	$31.8 \pm 1.8 \pm 0.8$	$-24.0 \pm 1.2 \pm 2.5$	$37.6 \pm 1.9 \pm 2.5$	$-19.8 \pm 1.2 \pm 4.6$	$34.7 \pm 1.8 \pm 3.3$
0.4	$-9.4 \pm 1.1 \pm 0.9$	$30.1 \pm 1.4 \pm 0.9$	$-19.7 \pm 1.1 \pm 3.1$	$34.8 \pm 1.3 \pm 3.0$	$-14.6 \pm 1.1 \pm 5.5$	$32.5 \pm 1.3 \pm 3.1$
0.5	$10.5 \pm 1.2 \pm 0.9$	$30.6 \pm 1.5 \pm 0.9$	$-4.6 \pm 1.3 \pm 3.4$	$36.9 \pm 1.6 \pm 3.0$	$3.0 \pm 1.2 \pm 7.9$	$33.8 \pm 1.5 \pm 3.7$
0.65	$19.5 \pm 1.3 \pm 1.0$	$27.6 \pm 1.3 \pm 1.0$	$5.4 \pm 1.2 \pm 3.4$	$35.2 \pm 1.2 \pm 3.4$	$12.4 \pm 1.2 \pm 7.4$	$31.4 \pm 1.2 \pm 4.4$
0.9	$31.9 \pm 2.6 \pm 4.3$	$30.6 \pm 2.1 \pm 4.3$	$18.7 \pm 2.7 \pm 4.3$	$36.2 \pm 2.1 \pm 4.2$	$25.3 \pm 2.7 \pm 7.9$	$33.4 \pm 2.1 \pm 5.1$
1.72	$72.5 \pm 1.0 \pm 4.4$	$24.8 \pm 1.4 \pm 5.4$	$58.5 \pm 1.1 \pm 4.3$	$26.9 \pm 1.3 \pm 5.4$	$65.5 \pm 1.0 \pm 8.3$	$25.8 \pm 1.3 \pm 5.5$
2.05	$72.0 \pm 0.9 \pm 4.3$	$21.0 \pm 1.7 \pm 5.1$	$62.9 \pm 0.9 \pm 3.4$	$15.5 \pm 1.5 \pm 5.0$	$67.4 \pm 0.9 \pm 6.0$	$18.2 \pm 1.6 \pm 5.8$
2.44	$50.0 \pm 1.0 \pm 3.4$	$9.3 \pm 1.3 \pm 4.3$	$56.2 \pm 0.9 \pm 3.4$	$11.8 \pm 1.4 \pm 4.3$	$53.1 \pm 1.0 \pm 4.6$	$10.6 \pm 1.4 \pm 4.5$
2.91	$37.5 \pm 1.1 \pm 3.0$	$9.8 \pm 2.0 \pm 2.6$	$42.5 \pm 1.1 \pm 3.0$	$13.8 \pm 2.1 \pm 2.6$	$40.0 \pm 1.1 \pm 3.9$	$11.8 \pm 2.1 \pm 3.3$
3.48	$29.6 \pm 0.8 \pm 2.9$	$4.2 \pm 2.5 \pm 2.6$	$32.6 \pm 0.9 \pm 2.8$	$14.1 \pm 2.4 \pm 2.4$	$31.1 \pm 0.9 \pm 3.2$	$9.1 \pm 2.5 \pm 5.5$
4.16	$19.3 \pm 2.0 \pm 4.0$	$10.8 \pm 2.8 \pm 4.7$	$23.1 \pm 2.2 \pm 4.9$	$17.5 \pm 2.6 \pm 5.6$	$21.2 \pm 2.1 \pm 4.9$	$14.1 \pm 2.7 \pm 6.1$

TABLE X. Results for the $\gamma^* p \to N(1535)S_{11}$ helicity amplitudes in units of 10^{-3} GeV$^{-1/2}$. The amplitudes are extracted from the data on $\gamma^* p \to \pi N$ using $\beta_{\pi N}(N(1535)S_{11}) = 0.485$ (see Sec. VII C). The remaining legend is as for Table IX.

Q^2 (GeV^2)	DR		UIM		Final results	
	$A_{1/2}$	$S_{1/2}$	$A_{1/2}$	$S_{1/2}$	$A_{1/2}$	$S_{1/2}$
0.3	$89.4 \pm 2.1 \pm 1.3$	$-11.0 \pm 2.1 \pm 0.9$	$90.9 \pm 2.3 \pm 1.8$	$-13.0 \pm 2.2 \pm 2.1$	$90.2 \pm 2.2 \pm 1.7$	$-12.0 \pm 2.2 \pm 1.8$
0.4	$90.6 \pm 1.7 \pm 1.4$	$-9.5 \pm 1.9 \pm 0.9$	$92.9 \pm 1.6 \pm 2.2$	$-15.9 \pm 2.0 \pm 2.2$	$91.8 \pm 1.7 \pm 2.1$	$-12.7 \pm 2.0 \pm 3.6$
0.5	$90.5 \pm 1.9 \pm 1.6$	$-10.8 \pm 2.2 \pm 1.2$	$91.7 \pm 2.0 \pm 2.7$	$-16.7 \pm 2.4 \pm 2.4$	$91.1 \pm 2.0 \pm 2.2$	$-13.8 \pm 2.3 \pm 3.5$
0.65	$90.0 \pm 1.7 \pm 1.8$	$-12.9 \pm 1.8 \pm 1.0$	$91.6 \pm 1.8 \pm 3.3$	$-14.4 \pm 1.9 \pm 2.3$	$90.8 \pm 1.8 \pm 2.7$	$-13.6 \pm 1.9 \pm 1.8$
0.9	$83.3 \pm 2.4 \pm 4.9$	$-11.2 \pm 3.8 \pm 4.6$	$85.5 \pm 2.3 \pm 5.2$	$-16.4 \pm 3.9 \pm 4.9$	$84.4 \pm 2.4 \pm 5.2$	$-13.8 \pm 3.9 \pm 5.5$
1.72	$72.2 \pm 1.5 \pm 5.0$	$-20.4 \pm 1.8 \pm 3.5$	$75.7 \pm 1.4 \pm 4.9$	$-24.8 \pm 1.6 \pm 3.3$	$73.9 \pm 1.5 \pm 5.2$	$-22.6 \pm 1.7 \pm 4.0$
2.05	$59.8 \pm 1.6 \pm 4.0$	$-14.8 \pm 2.0 \pm 3.9$	$65.4 \pm 1.7 \pm 4.0$	$-19.9 \pm 1.9 \pm 4.4$	$62.6 \pm 1.7 \pm 4.9$	$-17.4 \pm 1.9 \pm 4.9$
2.44	$54.5 \pm 2.1 \pm 3.6$	$-11.3 \pm 2.7 \pm 4.1$	$59.8 \pm 2.2 \pm 3.9$	$-16.7 \pm 2.9 \pm 4.3$	$57.2 \pm 2.2 \pm 4.6$	$-14.0 \pm 2.8 \pm 5.0$
2.91	$49.6 \pm 2.0 \pm 4.0$	$-9.0 \pm 2.6 \pm 2.9$	$53.0 \pm 1.9 \pm 4.5$	$-12.6 \pm 2.8 \pm 4.2$	$51.3 \pm 2.0 \pm 4.6$	$-10.8 \pm 2.7 \pm 4.0$
3.48	$44.9 \pm 2.2 \pm 4.2$	$-6.3 \pm 3.2 \pm 2.7$	$41.0 \pm 2.4 \pm 4.6$	$-11.3 \pm 3.4 \pm 2.8$	$43.0 \pm 2.3 \pm 4.8$	$-8.8 \pm 3.3 \pm 3.7$
4.16	$35.5 \pm 3.8 \pm 4.5$	$-4.5 \pm 6.2 \pm 3.5$	$31.8 \pm 3.6 \pm 4.5$	$-8.9 \pm 5.9 \pm 3.8$	$33.7 \pm 3.7 \pm 4.9$	$-6.7 \pm 6.0 \pm 4.3$

increases up to 3.2–3.3% at $Q^2 = 3$–6 GeV^2. For $M_{1+}^{3/2}$, the fit error given in Table VI includes the overall normalization error added in quadrature to the fit error.

Examples of the comparison with the experimental data are presented in Figs. 3–9. The obtained values of χ^2 in the fit to the data are presented in Tables I–IV. The relatively large values of χ^2 for $\frac{d\sigma}{d\Omega}(\pi^0)$ at $Q^2 = 0.16$ and $0.2\,\text{GeV}^2$ and for $\frac{d\sigma}{d\Omega}(\pi^+)$ at $Q^2 = 0.3$ and $0.4\,\text{GeV}^2$ and $Q^2 = 1.72$ and $2.05\,\text{GeV}^2$ are caused by small statistical errors, which for the corresponding data sets from Refs. [6], [4], and [7], increase with increasing Q^2. The values of χ^2 for $A_{LT'}$ at $Q^2 \geqslant 1.72$ GeV^2 are somewhat large. However, as demonstrated in Figs. 5 and 6, the description on the whole is satisfactory.

The comparison with the data for $\frac{d\sigma}{d\Omega}$ and $A_{LT'}$ is made in terms of the structure functions $\sigma_T + \epsilon\sigma_L$, σ_{TT}, σ_{LT}, $\sigma_{LT'}$ and their Legendre moments. They are defined in the following way:

$$\frac{d\sigma}{d\Omega} = \sigma_T + \epsilon\sigma_L + \epsilon\sigma_{TT}\cos 2\phi + \sqrt{2\epsilon(1+\epsilon)}\sigma_{LT}\cos\phi + h\sqrt{2\epsilon(1-\epsilon)}\sigma_{LT'}\sin\phi, \tag{16}$$

where $\frac{d\sigma}{d\Omega}$ is the differential cross section of the reaction $\gamma^* N \to N\pi$ in its c.m. system, assuming that the virtual photon flux factor is

$$\Gamma = \frac{\alpha}{2\pi^2 Q^2}\frac{(W^2 - m^2)E_f}{2mE_i}\frac{1}{1-\epsilon},$$

E_i, E_f are the initial and final electron energies in the laboratory frame, and ϵ is the polarization factor of the virtual photon. θ and ϕ are the polar and azimuthal angles of the pion in the c.m. system of the reaction $\gamma^* N \to N\pi$, and h is the electron helicity. The longitudinally polarized beam asymmetry is related to the structure function $\sigma_{LT'}$ by

$$A_{LT'} = \frac{\sqrt{2\epsilon(1-\epsilon)}\sigma_{LT'}\sin\phi}{\frac{d\sigma}{d\Omega}(h=0)}. \tag{17}$$

For the longitudinal target asymmetry A_t and beam-target asymmetry A_{et}, we use the relations presented in detail in Ref. [8], where the experimental results on these observables are reported. These relations express A_t and A_{et} through the response functions defined in Ref. [72].

TABLE XI. Results for the $\gamma^* p \to N(1520)D_{13}$ helicity amplitudes in units of 10^{-3} GeV$^{-1/2}$. The remaining legend is as for Table IX.

Q^2 (GeV^2)	DR			UIM		
	$A_{1/2}$	$A_{3/2}$	$S_{1/2}$	$A_{1/2}$	$A_{3/2}$	$S_{1/2}$
0.3	$-51.8 \pm 1.9 \pm 0.8$	$77.2 \pm 2.2 \pm 0.7$	$-43.7 \pm 2.4 \pm 1.0$	$-54.1 \pm 1.8 \pm 1.8$	$75.1 \pm 2.2 \pm 2.1$	$-48.4 \pm 2.4 \pm 2.3$
0.4	$-57.0 \pm 1.4 \pm 0.9$	$70.5 \pm 1.8 \pm 0.7$	$-39.7 \pm 1.9 \pm 1.0$	$-59.7 \pm 2.1 \pm 2.4$	$67.6 \pm 1.9 \pm 2.2$	$-43.6 \pm 2.1 \pm 2.4$
0.5	$-60.2 \pm 2.0 \pm 0.9$	$56.9 \pm 1.7 \pm 0.8$	$-35.5 \pm 2.5 \pm 0.8$	$-60.6 \pm 2.2 \pm 2.5$	$60.0 \pm 1.9 \pm 2.4$	$-39.4 \pm 2.4 \pm 2.8$
0.65	$-66.0 \pm 1.6 \pm 1.1$	$52.0 \pm 1.4 \pm 0.8$	$-32.7 \pm 2.1 \pm 0.7$	$-64.5 \pm 1.8 \pm 2.7$	$54.2 \pm 1.6 \pm 2.8$	$-37.5 \pm 1.9 \pm 2.5$
0.9	$-58.9 \pm 2.4 \pm 2.7$	$44.8 \pm 2.6 \pm 2.8$	$-29.0 \pm 3.3 \pm 2.5$	$-64.9 \pm 2.2 \pm 2.9$	$44.1 \pm 2.6 \pm 3.1$	$-34.3 \pm 3.1 \pm 3.0$
1.72	$-42.4 \pm 1.2 \pm 3.2$	$18.7 \pm 1.2 \pm 3.2$	$-11.8 \pm 1.1 \pm 3.1$	$-38.8 \pm 1.3 \pm 3.9$	$21.4 \pm 1.2 \pm 3.5$	$-9.1 \pm 1.0 \pm 1.8$
2.05	$-37.3 \pm 1.4 \pm 2.1$	$15.6 \pm 1.5 \pm 2.3$	$-9.6 \pm 1.6 \pm 2.8$	$-39.7 \pm 1.5 \pm 3.2$	$18.3 \pm 1.6 \pm 2.6$	$-6.8 \pm 1.5 \pm 1.9$
2.44	$-36.4 \pm 1.3 \pm 2.4$	$11.2 \pm 1.6 \pm 2.1$	$-5.5 \pm 1.8 \pm 1.6$	$-36.3 \pm 1.4 \pm 2.6$	$13.4 \pm 1.7 \pm 1.9$	$-3.6 \pm 1.9 \pm 1.6$
2.91	$-32.8 \pm 1.8 \pm 2.6$	$5.8 \pm 2.1 \pm 2.9$	$-3.3 \pm 2.0 \pm 1.5$	$-31.0 \pm 1.9 \pm 2.2$	$9.6 \pm 2.0 \pm 2.7$	$-2.3 \pm 2.1 \pm 1.6$
3.48	$-22.4 \pm 2.1 \pm 2.7$	$5.5 \pm 2.0 \pm 5.5$	$-5.3 \pm 2.5 \pm 2.0$	$-24.9 \pm 2.2 \pm 2.9$	$8.2 \pm 2.2 \pm 5.2$	$-2.6 \pm 2.6 \pm 2.4$
4.16	$-19.1 \pm 3.9 \pm 3.0$	$6.4 \pm 3.0 \pm 7.5$	$-2.6 \pm 4.8 \pm 3.0$	$-20.9 \pm 4.2 \pm 3.2$	$4.6 \pm 3.2 \pm 6.9$	$-0.7 \pm 4.6 \pm 3.2$

TABLE XII. Average values of the $\gamma^* p \to N(1520)D_{13}$ helicity amplitudes found using DR and UIM (in units of 10^{-3} GeV$^{-1/2}$). The first uncertainty is statistical; the second one is the model uncertainty discussed in Sec. VI.

Q^2 (GeV^2)	$A_{1/2}$	$A_{3/2}$	$S_{1/2}$
0.3	$-52.9 \pm 1.8 \pm 1.7$	$76.1 \pm 2.2 \pm 1.7$	$-46.1 \pm 2.4 \pm 2.9$
0.4	$-58.3 \pm 1.8 \pm 2.1$	$69.1 \pm 1.8 \pm 2.1$	$-41.7 \pm 2.0 \pm 2.6$
0.5	$-60.4 \pm 2.1 \pm 1.7$	$58.5 \pm 1.8 \pm 2.2$	$-37.5 \pm 2.5 \pm 2.7$
0.65	$-65.2 \pm 1.7 \pm 2.0$	$53.1 \pm 1.5 \pm 2.1$	$-35.1 \pm 2.0 \pm 2.9$
0.9	$-61.9 \pm 2.3 \pm 4.1$	$44.4 \pm 2.6 \pm 3.0$	$-31.6 \pm 3.2 \pm 3.8$
1.72	$-40.6 \pm 1.2 \pm 4.0$	$20.0 \pm 1.2 \pm 3.6$	$-10.5 \pm 1.0 \pm 2.8$
2.05	$-38.5 \pm 1.5 \pm 2.9$	$17.0 \pm 1.5 \pm 2.8$	$-8.2 \pm 1.5 \pm 2.7$
2.44	$-36.3 \pm 1.3 \pm 2.5$	$12.3 \pm 1.7 \pm 2.3$	$-4.6 \pm 1.8 \pm 1.9$
2.91	$-31.9 \pm 1.8 \pm 2.6$	$7.7 \pm 2.0 \pm 3.4$	$-2.8 \pm 2.0 \pm 1.6$
3.48	$-23.6 \pm 2.2 \pm 3.1$	$6.8 \pm 2.1 \pm 5.5$	$-4.0 \pm 2.5 \pm 2.6$
4.16	$-20.0 \pm 4.1 \pm 3.2$	$5.5 \pm 3.1 \pm 7.3$	$-1.6 \pm 4.7 \pm 3.2$

The Legendre moments of the structure functions are defined as the coefficients in the expansion of these functions over Legendre polynomials $P_l(\cos\theta)$:

$$\sigma_T(W,\cos\theta) + \epsilon\sigma_L(W,\cos\theta) = \sum_{l=0}^{n} D_l^{T+L}(W) P_l(\cos\theta), \tag{18}$$

$$\sigma_{LT}(W,\cos\theta) = \sin\theta \sum_{l=0}^{n-1} D_l^{LT}(W) P_l(\cos\theta), \tag{19}$$

$$\sigma_{LT'}(W,\cos\theta) = \sin\theta \sum_{l=0}^{n-1} D_l^{LT'}(W) P_l(\cos\theta), \tag{20}$$

$$\sigma_{TT}(W,\cos\theta) = \sin^2\theta \sum_{l=0}^{n-2} D_l^{TT}(W) P_l(\cos\theta). \tag{21}$$

The Legendre moments allow us to present a comparison of the results with the data over all energies and angles in compact form.

The Legendre moment D_0^{T+L} represents the $\cos\theta$ independent part of $\sigma_T + \epsilon\sigma_L$, which is related to the $\gamma^* N \to \pi N$ total cross section:

$$\begin{aligned} D_0^{T+L} &= \frac{1}{4\pi}\left(\sigma_{\rm tot}^T + \epsilon\sigma_{\rm tot}^L\right) \equiv \frac{|\mathbf{q}|}{K}\left(\tilde\sigma_{\rm tot}^T + \epsilon\tilde\sigma_{\rm tot}^L\right), \\ \tilde\sigma_{\rm tot}^T &= \tilde\sigma_{1/2} + \tilde\sigma_{3/2}, \\ \tilde\sigma_{1/2} &= \sum_{l=0}^{\infty}(l+1)(|A_{l+}|^2 + |A_{(l+1)-}|^2), \\ \tilde\sigma_{3/2} &= \sum_{l=1}^{\infty}\frac{l}{4}(l+1)(l+2)(|B_{l+}|^2 + |B_{(l+1)-}|^2), \\ \tilde\sigma_{\rm tot}^L &= \frac{Q^2}{\mathbf{k}^2}\sum_{l=0}^{\infty}(l+1)^3(|S_{l+}|^2 + |S_{(l+1)-}|^2). \end{aligned} \tag{22}$$

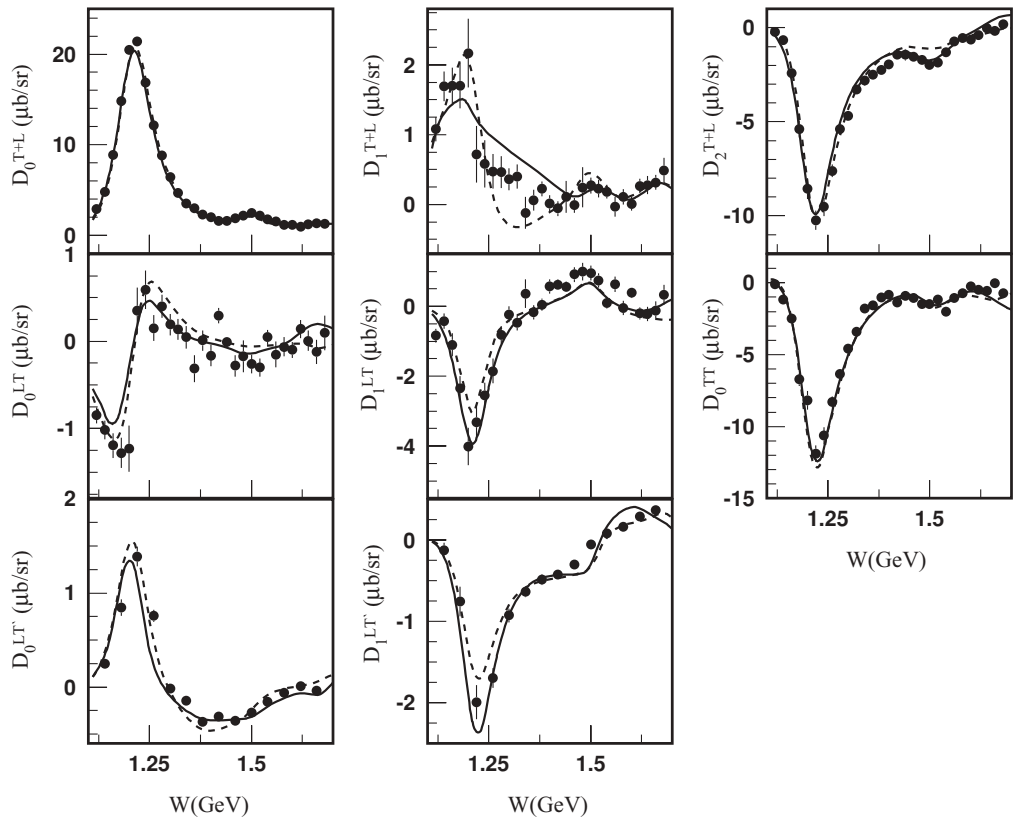

FIG. 3. Our results for the Legendre moments of the $\vec{e}p \to ep\pi^0$ structure functions in comparison with experimental data [1] for $Q^2 = 0.4$ GeV^2. The solid (dashed) curves correspond to the results obtained using the DR (UIM) approach.

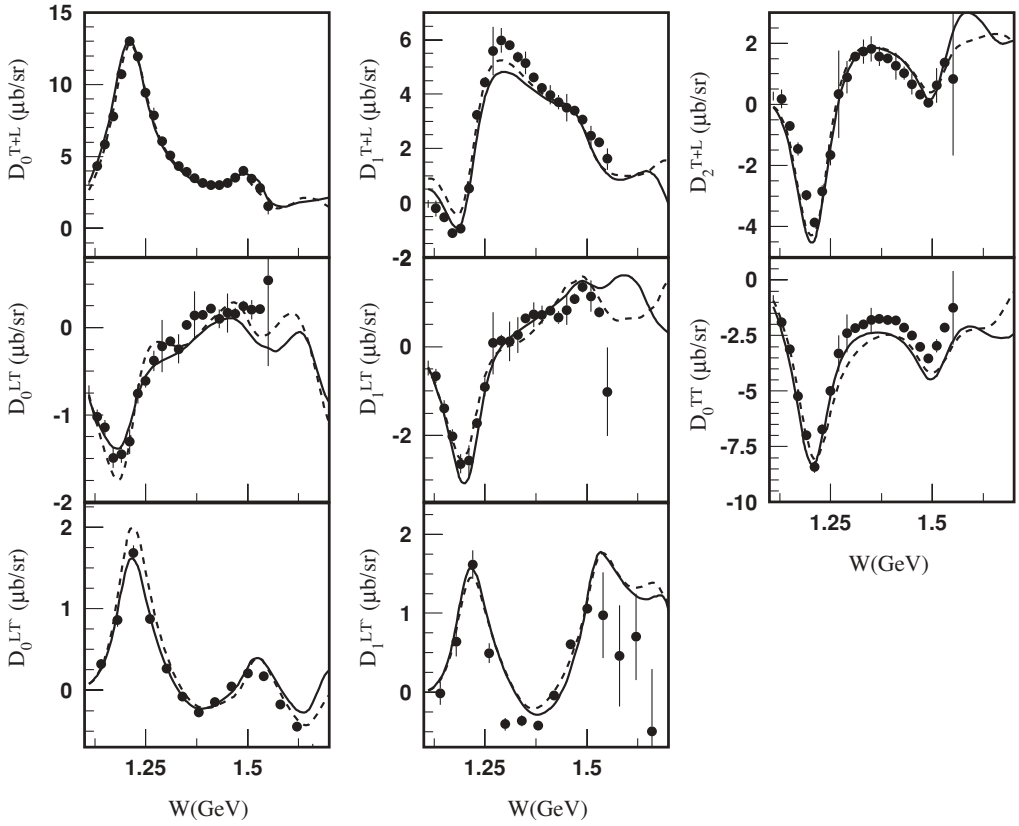

FIG. 4. Our results for the Legendre moments of the $\vec{e}p \to en\pi^+$ structure functions in comparison with experimental data [4] for $Q^2 = 0.4$ GeV^2. The solid (dashed) curves correspond to the results obtained using the DR (UIM) approach.

Here $\mathbf{q}$ and $\mathbf{k}$ are, respectively, the pion and virtual photon three-momenta in the c.m. system of the reaction $\gamma^* N \to \pi N$, $K = (W^2 - m^2)/2W$, and

$$\begin{aligned} A_{l+} &= \tfrac{1}{2}[(l+2)E_{l+} + lM_{l+}], \\ B_{l+} &= E_{l+} - M_{l+}, \\ A_{(l+1)-} &= \tfrac{1}{2}[(l+2)M_{(l+1)-} - lE_{(l+1)-}], \\ B_{(l+1)-} &= E_{(l+1)-} + M_{(l+1)-}. \end{aligned} \tag{23}$$

The resonance structures related to the resonances $\Delta(1232)P_{33}$, $N(1520)D_{13}$, and $N(1535)S_{11}$ are revealed in D_0^{T+L} as enhancements. It can be seen that with increasing Q^2, the resonant structure near 1.5 GeV becomes increasingly dominant in comparison with the $\Delta(1232)$. At $Q^2 \geqslant 1.72$ GeV^2, there is a shoulder between the Δ and 1.5 GeV peaks, which is related to the large contribution of the broad Roper resonance. As can be seen from Table IX, the transverse helicity amplitude $A_{1/2}$ for $\gamma^* p \to N(1440)P_{11}$, which is large and negative at $Q^2 = 0$ [20], crosses zero between $Q^2 = 0.4$ and 0.65 GeV^2 and becomes large and positive at $Q^2 = 1.72$ GeV^2. With increasing Q^2, this amplitude drops smoothly in magnitude.

There are dips in the Legendre moment D_2^{T+L} that are caused by the $\Delta(1232)P_{33}$ and the $N(1520)D_{13}$ and $N(1535)S_{11}$ resonances. They are related to the following contributions to D_2^T:

$$D_2^T = -\frac{|\mathbf{q}|}{K}[4Re(A_{0+}A_{2-}^*) + |M_{1+}|^2]. \tag{24}$$

When Q^2 grows, the dip related to the $\Delta(1232)P_{33}$ resonance becomes smaller than that near 1.5 GeV.

At $Q^2 > 1.72$ GeV^2, the relative values of the dip in D_2^{T+L} and the enhancement in D_0^{T+L} near 1.5 GeV, and the shoulder between the Δ and 1.5 GeV peaks in D_0^{T+L}, remain approximately the same with increasing Q^2. Our analysis shows that this is a manifestation of the slow falloff of the $A_{1/2}$ helicity amplitudes of the transitions $\gamma^* p \to N(1440)P_{11}, N(1535)S_{11}, N(1520)D_{13}$ for these Q^2.

The enhancement in D_0^{T+L} and the dip in D_0^{TT} in the Δ peak are mainly related to the $M_{1+}^{3/2}$ amplitude of the $\gamma^* p \to \Delta(1232)P_{33}$ transition:

$$D_0^{T+L} \approx 2\frac{|\mathbf{q}|}{K}|M_{1+}|^2, \tag{25}$$

$$D_0^{TT} \approx -\frac{3}{2}\frac{|\mathbf{q}|}{K}|M_{1+}|^2. \tag{26}$$

In Figs. 7–9, we show the results for the target and double-spin asymmetries for $\vec{e}\vec{p} \to ep\pi^0$ [8]. The inclusion of these data into the analysis resulted in a smaller magnitude of the $S_{1/2}$ amplitude for the Roper resonance and in larger $A_{1/2}$ and smaller $|S_{1/2}|$ amplitudes for the $\gamma^* p \to N(1535)S_{11}$

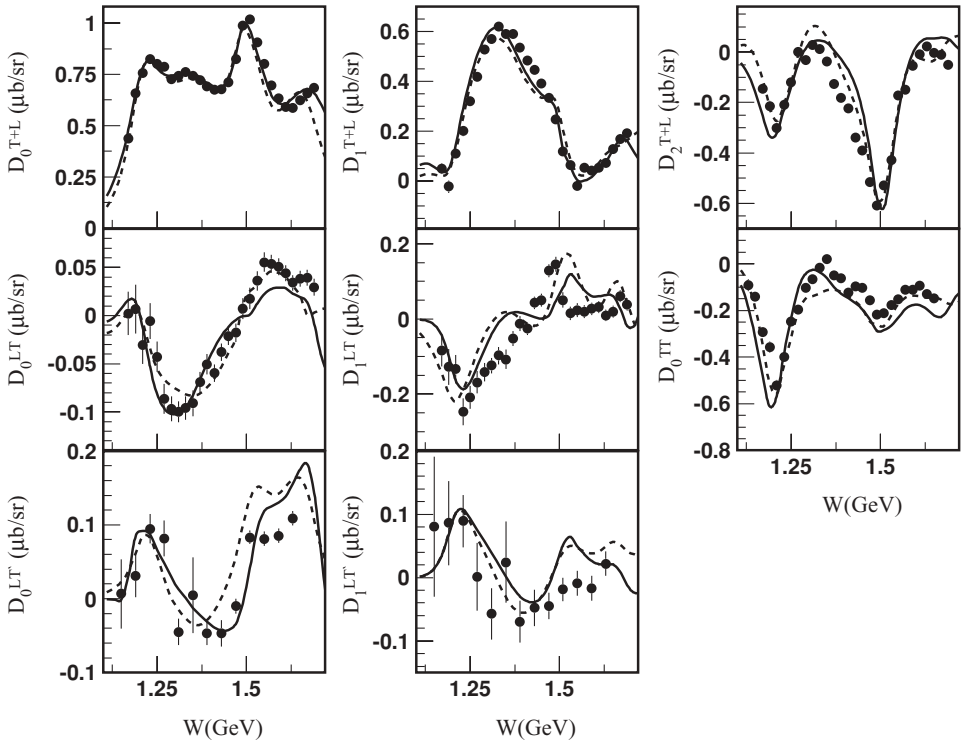

FIG. 5. Our results for the Legendre moments of the $\vec{e}p \to en\pi^+$ structure functions in comparison with experimental data [7] for $Q^2 = 2.44$ GeV^2. The solid (dashed) curves correspond to the results obtained using the DR (UIM) approach.

transition. These data had a minor impact on the $\gamma^* p \to \Delta(1232)P_{33}$ and $N(1520)D_{13}$ amplitudes.

VII. COMPARISON WITH THEORETICAL PREDICTIONS

In Figs. 10 and 13–15, we present our final results from Tables VI–X and XII; they are average values of the amplitudes extracted using DR and UIM.

A. $\Delta(1232)P_{33}$ resonance

The results for the $\gamma^* p \to \Delta(1232)P_{33}$ magnetic dipole form factor in the Ash convention [73] and for the ratios $R_{EM} \equiv E_{1+}^{3/2}/M_{1+}^{3/2}$ and $R_{SM} \equiv S_{1+}^{3/2}/M_{1+}^{3/2}$ are presented in Fig. 10. The relationship between $G^*_{M,\mathrm{Ash}}(Q^2)$ and the corresponding multipole amplitude is given by

$$G^*_{M,\mathrm{Ash}}(Q^2) = \frac{m}{k_r}\sqrt{\frac{8q_r\Gamma}{3\alpha}}M_{1+}^{3/2}(Q^2, W = M), \qquad (27)$$

where $M = 1232$ MeV and $\Gamma = 118$ MeV are the mean values of the mass and width of the $\Delta(1232)P_{33}$ (Table V), q_r and k_r are the pion and virtual photon three-momenta, respectively, in the c.m. system of the reaction $\gamma^* p \to p\pi^\circ$ at the $\Delta(1232)P_{33}$ resonance position, and m is the nucleon mass. This definition is related to the definition of G_M^* in the Jones-Scadron convention [74] by

$$G^*_{M,\mathrm{J-S}}(Q^2) = G^*_{M,\mathrm{Ash}}(Q^2)\sqrt{1 + \frac{Q^2}{(M+m)^2}}. \qquad (28)$$

The low-Q^2 data from Mainz Microtron (MAMI) [75,76] and the MIT Bates Linear Accelerator Center [77] and earlier results from JLab Hall C [78] and Hall A [79,80] are also shown in Fig. 10. The form factor $G_M^*(Q^2)$ is presented relative to the dipole form factor, which approximately describes the elastic magnetic form factor of the proton. The plot shows that new exclusive measurements of $G_M^*(Q^2)$, which now extend over the range $Q^2 = 0.06$–6 GeV^2, confirm the rapid falloff of $G_M^*(Q^2)$ relative to the proton magnetic form factor seen previously in inclusive measurements.

Figure 10 shows the long-standing discrepancy between the measured $G_M^*(Q^2)$ and the constituent quark model predictions; here they are in comparison with the LF relativistic quark model of Ref. [18]. Within dynamical reaction models [25–28], the meson-cloud contribution was identified as the source of this discrepancy. The importance of the pion (cloud) contribution for the $\gamma^* p \to \Delta(1232)P_{33}$ transition is confirmed also by the lattice QCD calculations [29]. In Fig. 10, the results of the dynamical model of Ref. [27] are plotted. They show the total amplitude ("dressed" form factor) and the amplitude with the subtracted meson-cloud contribution ("bare" form factor). Very close results are obtained within the dynamical model of Refs. [25,26]. The meson-cloud contribution makes up more than 30% of the total amplitude at the photon point and remains sizable while Q^2 increases.

Figure 10 also shows the prediction [37] obtained in the large-N_c limit of QCD, by relating the $N \to \Delta$ and $N \to N$ GPDs. A quantitative description of $G_M^*(Q^2)$ is obtained in the whole Q^2 range.

A consistent picture emerges from the data for the ratios R_{EM} and R_{SM} : R_{EM} remains negative, small, and nearly

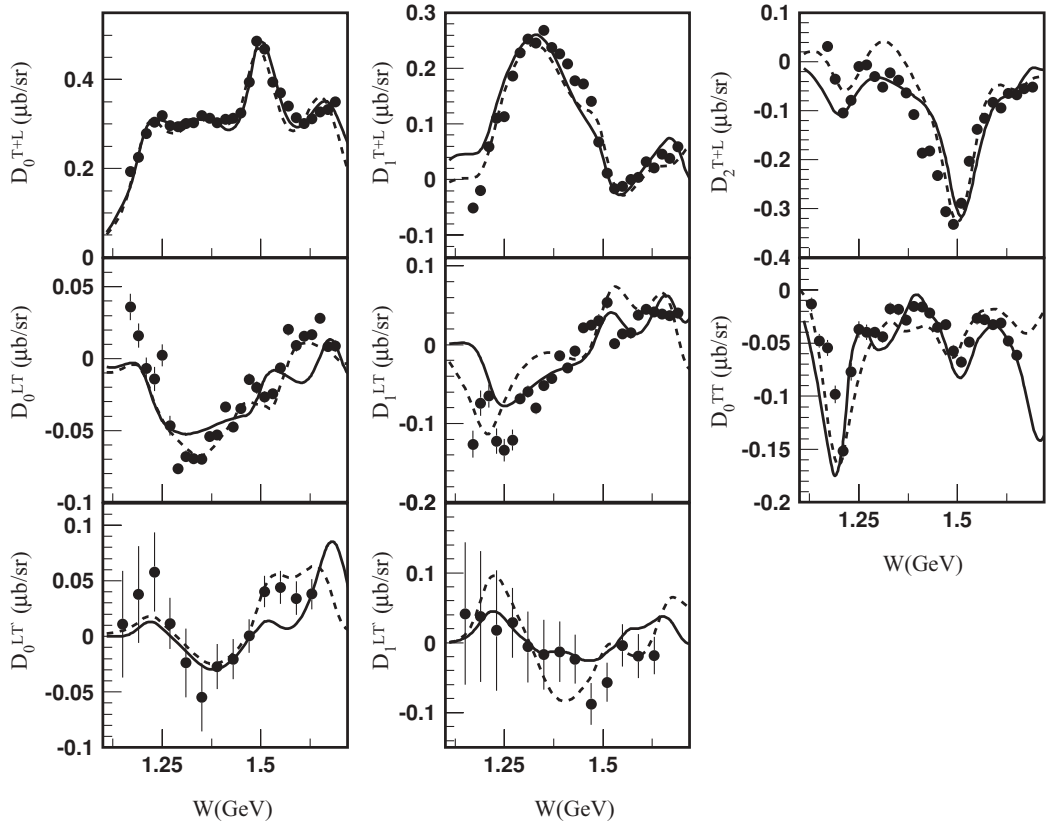

FIG. 6. Same as in Fig. 5, but for $Q^2 = 3.48$ GeV^2.

constant in the entire range $0 < Q^2 < 6$ GeV^2; R_{SM} remains negative, but its magnitude strongly rises at high Q^2. It should be mentioned that the observed behavior of R_{SM} at large Q^2 sharply disagrees with the solution of MAID2007 [39] based on the same data set. The magnitude of the relevant amplitude $S_{1+}^{3/2}$ can be directly checked using the data for the structure function σ_{LT}, whose $\cos\theta$ behavior at $W = 1.23$ GeV is dominated by the interference of this amplitude

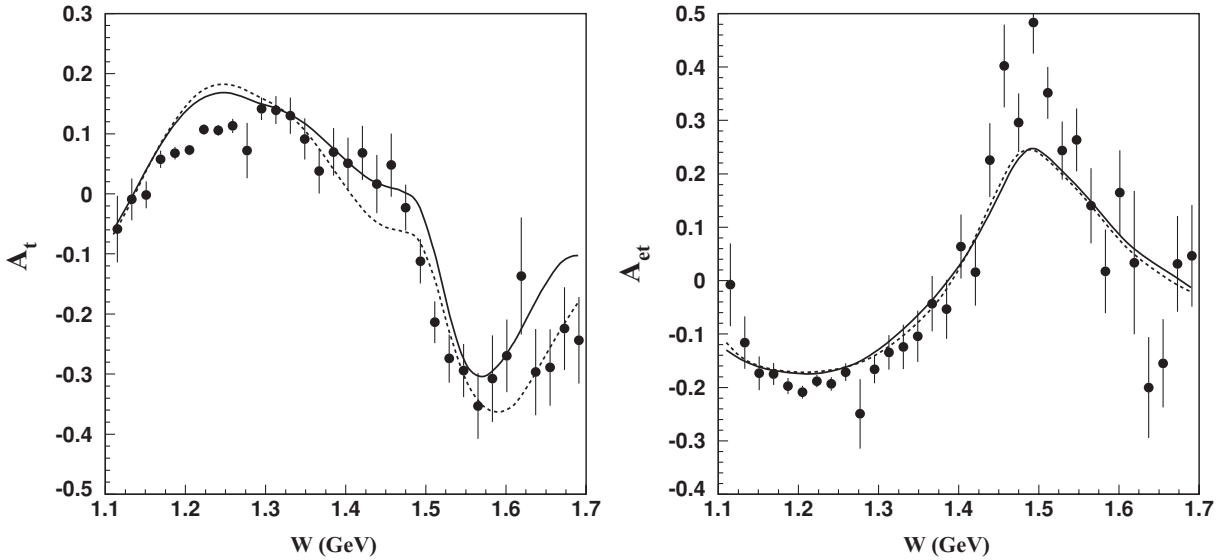

FIG. 7. A_t (left panel) and A_{et} (right panel) as functions of the invariant mass W, integrated over the whole range in $\cos\theta$, $0.252 < Q^2 < 0.611$ GeV^2 and $60^\circ < \phi < 156^\circ$. Experimental data are from Ref. [8]. Solid and dashed curves correspond to our results obtained using DR and UIM approaches, respectively.

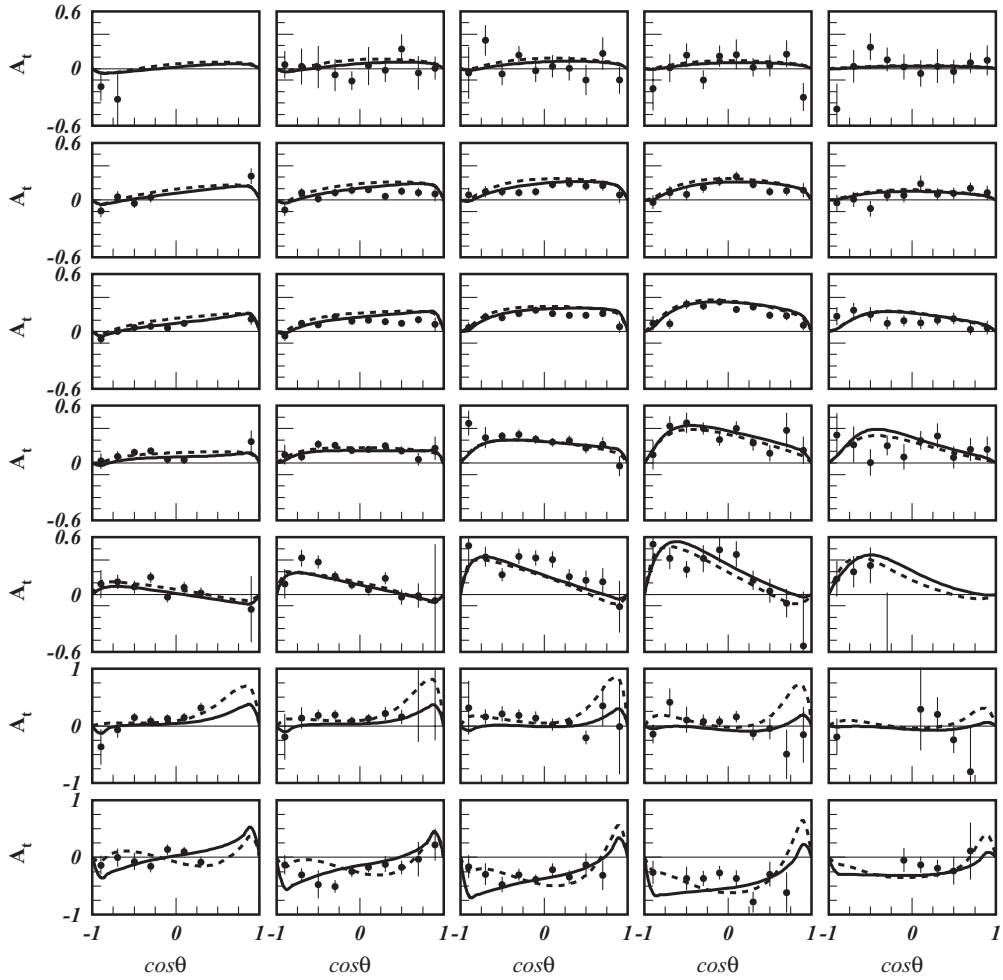

FIG. 8. Our results for the longitudinal target asymmetry A_t in comparison with experimental data for $Q^2 = 0.385$ GeV^2 [8]. Solid (dashed) curves correspond to the results obtained using the DR (UIM) approach. Rows correspond to seven W bins with W mean values of 1.125, 1.175, 1.225, 1.275, 1.35, 1.45, and 1.55 GeV. Columns correspond to ϕ bins with $\phi = \pm 72^\circ, \pm 96^\circ, \pm 120^\circ, \pm 144^\circ, \pm 168^\circ$. The solid circles are the average values of the data for positive ϕ and those at negative ϕ taken with opposite signs.

with $M_{1+}^{3/2}$:

$$D_1^{LT}(ep \to ep\pi^0) \approx \frac{8}{3}\left(S_{1+}^{3/2}\right)^* M_{1+}^{3/2}. \tag{29}$$

The comparison of the experimental data for the $ep \to ep\pi^0$ structure functions with our results and the MAID2007 solution is shown in Figs. 11 and 12. At $Q^2 = 0.4$–1.45 GeV^2 (Fig. 11), MAID2007 describes the angular behavior of σ_{LT}. However, it increasingly underestimates the strong $\cos\theta$ dependence of this structure function with rising Q^2, which is the direct consequence of the small values of R_{SM} in the MAID2007 solution. At $Q^2 \geqslant 3$ GeV^2, this is demonstrated in Fig. 12. In terms of χ^2 per data point for σ_{LT} at $W = 1.23$ GeV, the situation is presented in Table XIII.

In constituent quark models, the nonzero magnitude of $E_{1+}^{3/2}$ can arise only as the result of a deformation of the SU(6) spherical symmetry in the N and/or $\Delta(1232)$ wave functions. In this connection, it is interesting that both dynamical models [25,27] give practically zero bare values for R_{EM} (as well as for R_{SM}). The entire $E_{1+}^{3/2}$ amplitude in these models is due to the quadrupole deformation that arises through the interaction of the photon with the meson cloud.

The knowledge of the Q^2 behavior of the ratios R_{EM} and R_{SM} is of great interest as a measure of the Q^2 scale where the asymptotic domain of QCD may set in for this resonance transition. In the pQCD asymptotics, $R_{EM} \to 100\%$

TABLE XIII. Our results obtained within DR and UIM, and the results of the MAID2007 solution [39] for χ^2 per data point for σ_{LT} at $W = 1.23$ GeV for $ep \to ep\pi^0$ data [1,5].

Q^2 (GeV^2)	χ^2/d.p.		
	DR	UIM	MAID2007
0.4	2.0	2.3	2.6
0.75	1.3	1.8	1.3
1.45	0.9	1.1	1.0
3	1.6	1.9	4.8
4.2	1.5	1.8	2.9
5	1.0	1.3	2.6

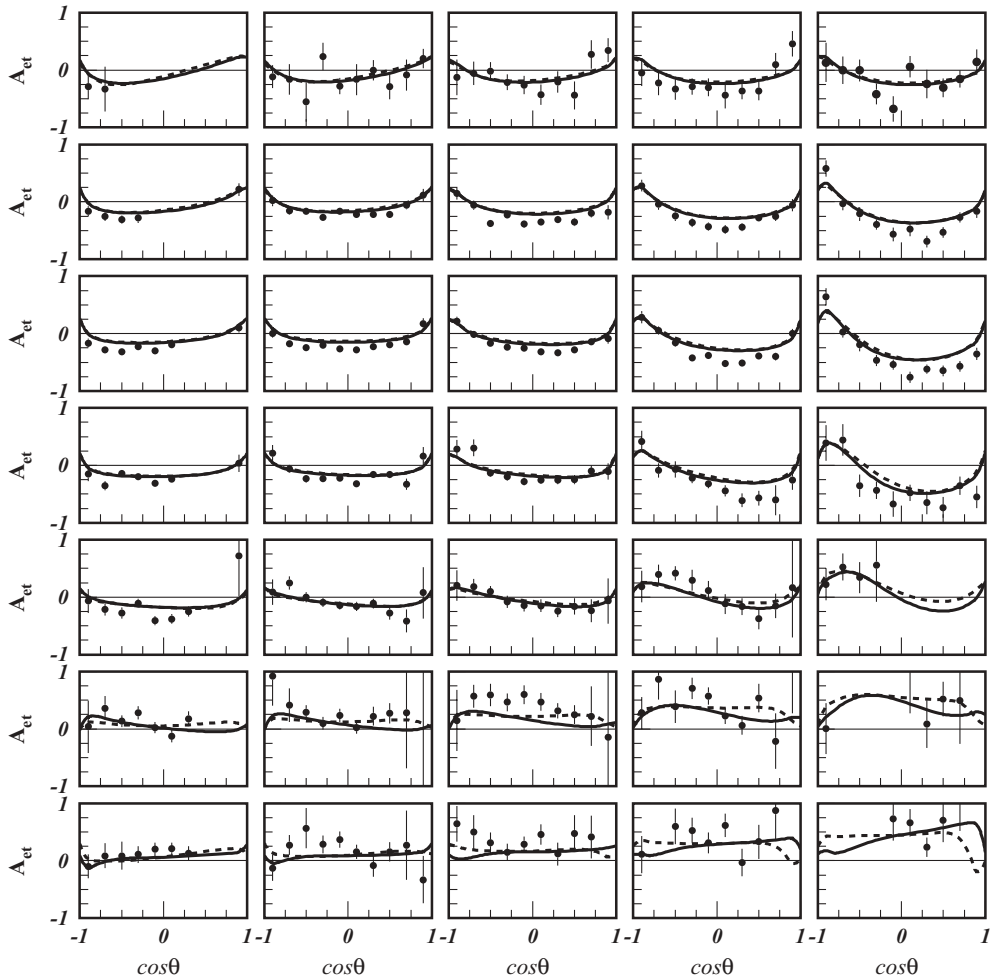

FIG. 9. Our results for the beam-target asymmetry A_{et} in comparison with experimental data for $Q^2 = 0.385$ GeV^2 [8]. Solid (dashed) curves correspond to the results obtained using the DR (UIM) approach. Rows correspond to seven W bins with W mean values of 1.125, 1.175, 1.225, 1.275, 1.35, 1.45, and 1.55 GeV. Columns correspond to ϕ bins with $\phi = \pm 72^\circ, \pm 96^\circ, \pm 120^\circ, \pm 144^\circ$, and $\pm 168^\circ$. The average values of the data for positive and negative ϕ are shown by solid circles.

and $R_{SM} \to$ const. The measured values of R_{EM} and R_{SM} show that in the range $Q^2 < 6$ GeV^2, there is no sign of an approach to the asymptotic pQCD regime in either of these ratios.

B. $N(1440)P_{11}$ resonance

The results for the $\gamma^* p \to N(1440)P_{11}$ helicity amplitudes are presented in Fig. 13. The high-Q^2 amplitudes ($Q^2 =$ 1.72–4.16 GeV^2) and the results for $Q^2 = 0.4$ and 0.65 GeV^2 were already presented and discussed in Refs. [41,82]. In the present paper, the data for $Q^2 = 0.4$ and 0.65 GeV^2 were reanalyzed taking into account the recent CLAS polarization measurements on the target and beam-target asymmetries [8]. Also included are new results extracted at $Q^2 = 0.3$, 0.525, and 0.9 GeV^2.

By quantum numbers, the most natural classification of the Roper resonance in the constituent quark model is a first radial excitation of the three-quark ($3q$) ground state. However, the difficulties of quark models in describing the low mass and large width of the $N(1440)P_{11}$, and also its photocouplings to the proton and neutron, gave rise to numerous speculations. Alternative descriptions of this state as a gluonic baryon excitation [30,31], or a hadronic $N\sigma$ molecule [33], were suggested. The CLAS measurements, for the first time, made possible the determination of the electroexcitation amplitudes of the Roper resonance on the proton up to $Q^2 = 4.5$ GeV^2. These results are crucial to understanding the nature of this state. There are several specific features in the extracted $\gamma^* p \to N(1440)P_{11}$ amplitudes that are very important to test models. First is the specific behavior of the transverse amplitude $A_{1/2}$, which being large and negative at $Q^2 = 0$, becomes large and positive at $Q^2 \simeq 2$ GeV^2, and then drops slowly with Q^2. Second is the relative sign between the longitudinal $S_{1/2}$ and transverse $A_{1/2}$ amplitudes. And third is the common sign of the amplitudes $A_{1/2}$ and $S_{1/2}$ extracted from the data on $\gamma^* p \to \pi N$, which includes signs from the $\gamma^* p \to N(1440)P_{11}$ and $N(1440)P_{11} \to \pi N$ vertices; both

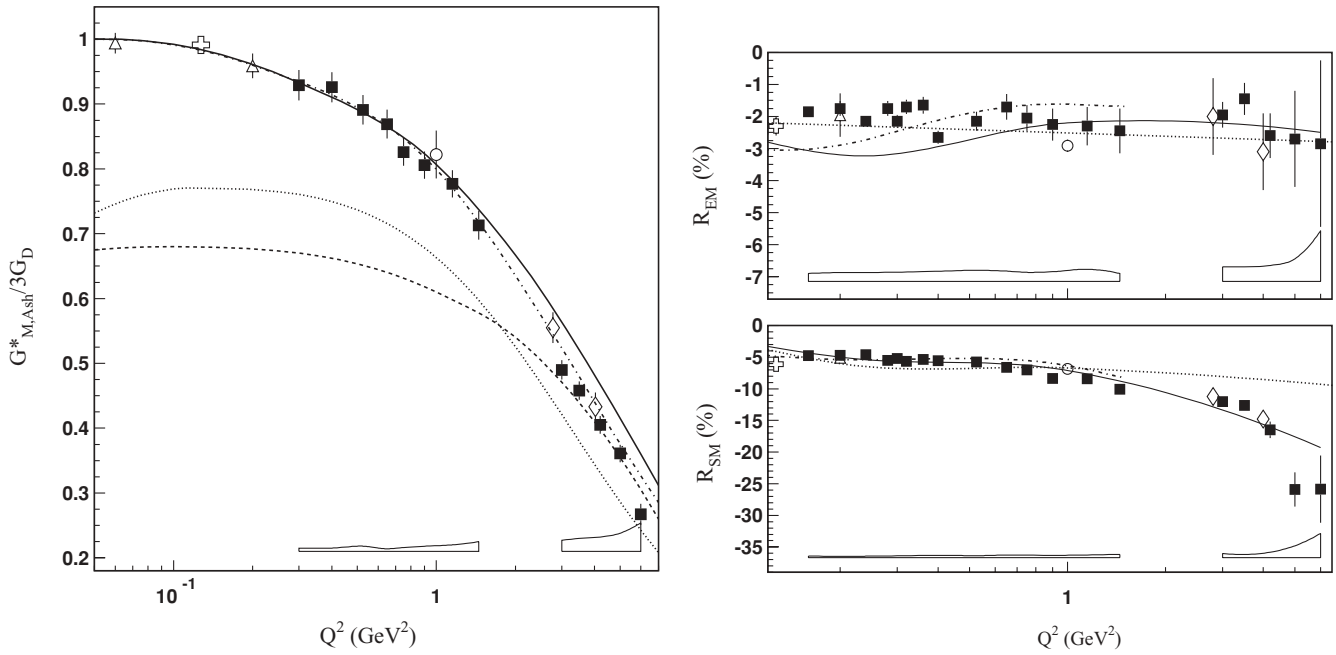

FIG. 10. Left panel: form factor G_M^* for the $\gamma^* p \to \Delta(1232)P_{33}$ transition relative to $3G_D$. Right panel: ratios R_{EM}, R_{SM}. The full boxes are the results from Tables VI–VIII obtained in this work from CLAS data (Tables I, III, and IV). The bands show the model uncertainties. Also shown are the results from MAMI [75,76] (open triangles), MIT Bates [77] (open crosses), JLab/Hall C [78] (open rhombuses), and JLab/Hall A [79,80] (open circles). The solid and dashed curves correspond to the dressed and bare contributions from Ref. [27]; for R_{EM}, R_{SM}, only the dressed contributions are shown; the bare contributions are close to zero. The dashed-dotted curves are the predictions obtained in the large-N_c limit of QCD [37,81]. The dotted curve for G_M^* is the prediction of a LF relativistic quark model of Ref. [18]; the dotted curves for R_{EM}, R_{SM} are the MAID2007 solutions [39].

signs should be taken into account while comparing with model predictions. All these characteristics are described by the light-front relativistic quark models of Refs. [15,19] assuming that $N(1440)P_{11}$ is the first radial excitation of the $3q$ ground state. Although the models [15,19] fail to describe numerically the data at small Q^2, this can have the natural explanation in the meson-cloud contributions, which are expected to be large for low Q^2 [83].

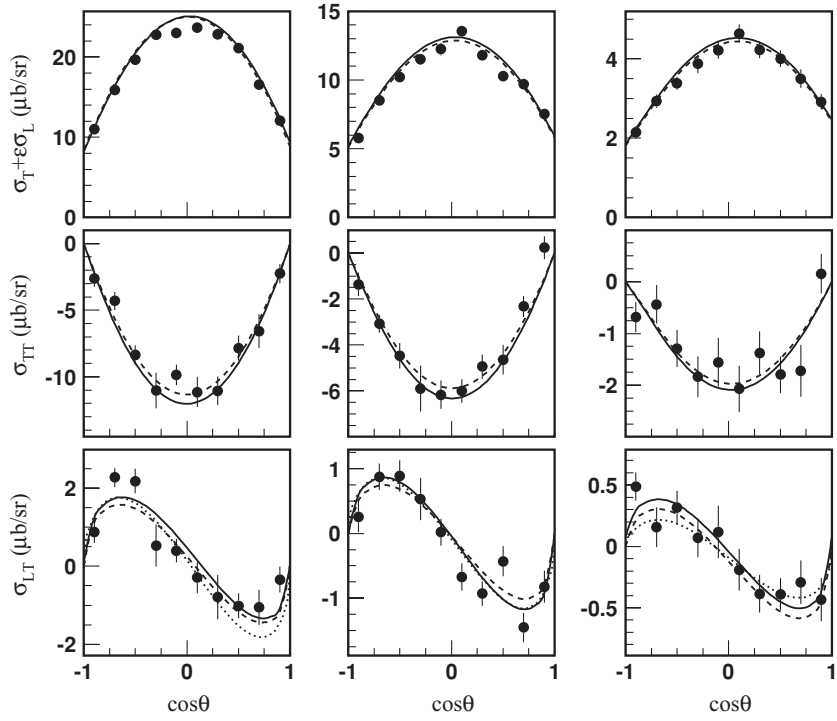

FIG. 11. Our results for the $ep \to ep\pi^0$ structure functions (in μb/sr units) in comparison with experimental data [1] for $W = 1.23$ GeV. The columns correspond to $Q^2 = 0.4$, 0.75, and 1.45 GeV^2. The solid (dashed) curves correspond to the results obtained using the DR (UIM) approach. The dotted curves are from MAID2007 [39].

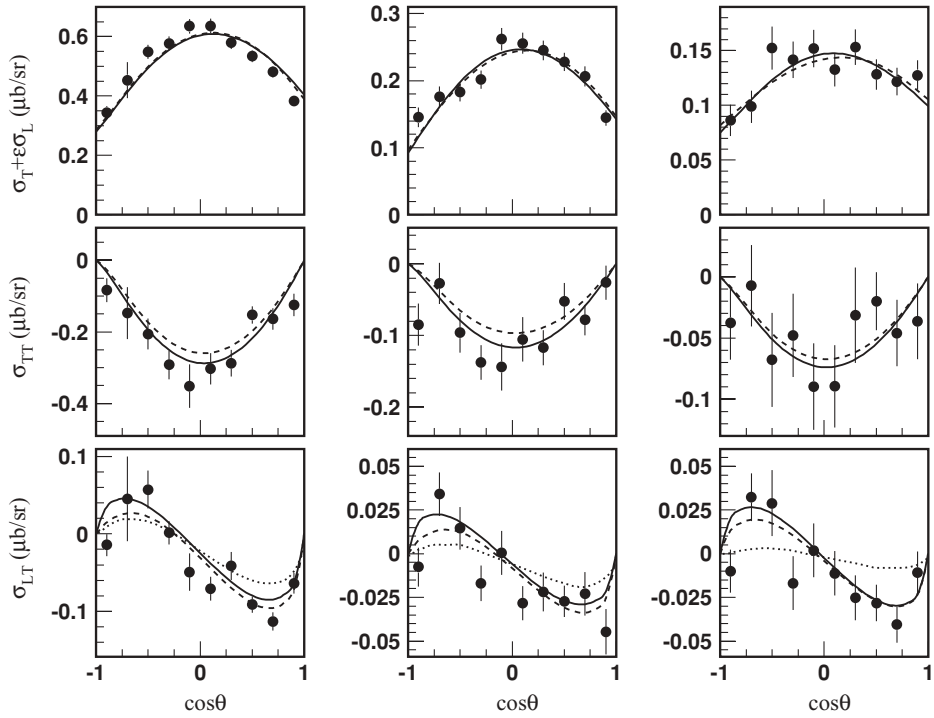

FIG. 12. Same as Fig. 11, but the columns correspond to $Q^2 = 3$, 4.2, 5 GeV^2.

C. $N(1535)S_{11}$ resonance

For the first time, the $\gamma^* N \to N(1535)S_{11}$ transverse helicity amplitude has been extracted from the π electroproduction data in a wide range of Q^2 (Fig. 14), and the results confirm the Q^2 dependence of this amplitude observed in η electroproduction. Numerical comparison of the results extracted from the π and η photoproduction and electroproduction data depends on the relation between the branching ratios to the πN and ηN channels. Consequently, it contains an arbitrariness connected with the uncertainties of these branching ratios: $\beta_{\pi N} = 0.35$–0.55, $\beta_{\eta N} = 0.45$–0.6 [20]. The amplitudes extracted from η photoproduction and electroproduction in Refs. [46–48,84] correspond to $\beta_{\eta N} = 0.55$.

The amplitudes found from π and η data can be used to specify the relation between $\beta_{\pi N}$ and $\beta_{\eta N}$. From the fit to these amplitudes at $0 \leqslant Q^2 < 4.5$ GeV^2, we found

$$\frac{\beta_{\eta N}}{\beta_{\pi N}} = 0.95 \pm 0.03. \tag{30}$$

Further, taking into account the branching ratio to the $\pi\pi N$ channel $\beta_{\pi\pi N} = 0.01$–0.1 [20], which accounts practically for

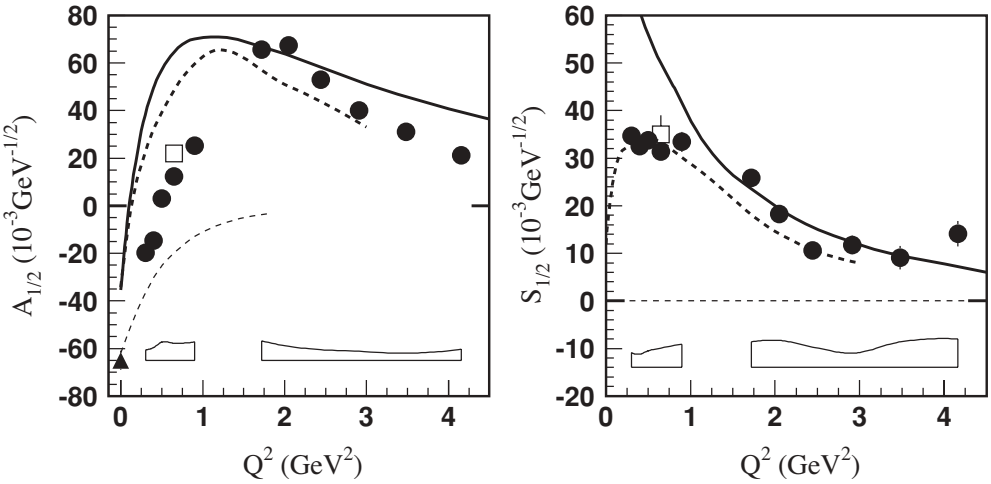

FIG. 13. Helicity amplitudes for the $\gamma^* p \to N(1440)P_{11}$ transition. The full circles are the results from Table IX obtained in this work from CLAS data (Tables I–IV). The bands show the model uncertainties. The open boxes are the results of the combined analysis of CLAS single π and 2π electroproduction data [42]. The full triangle at $Q^2 = 0$ is the RPP estimate [20]. The thick curves correspond to the results obtained in the LF relativistic quark models assuming that $N(1440)P_{11}$ is a first radial excitation of the $3q$ ground state: [15] (dashed), [19] (solid). The thin dashed curves are obtained assuming that $N(1440)P_{11}$ is a gluonic baryon excitation (q^3G hybrid state) [31].

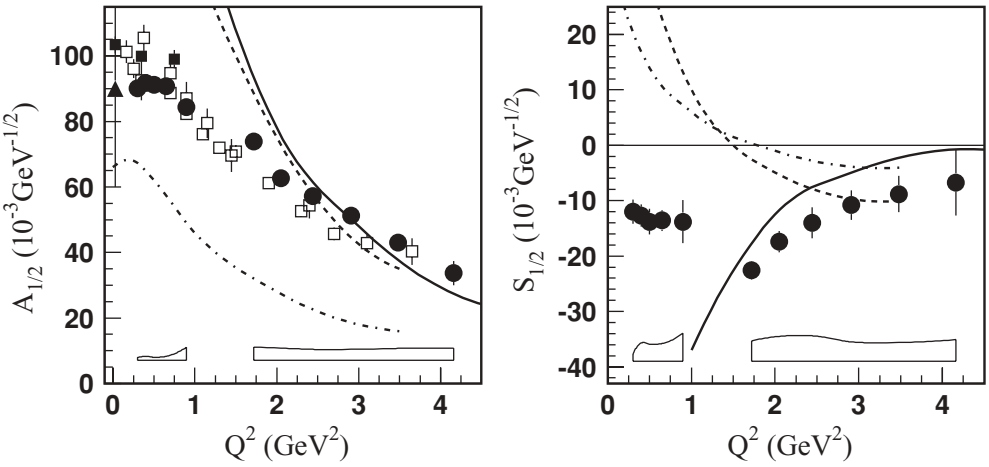

FIG. 14. Helicity amplitudes for the $\gamma^* p \to N(1535)S_{11}$ transition. The legend is partly as for Fig. 13. The solid boxes are the results extracted from η photo- and electroproduction data in Ref. [84], the open boxes show the results from η electroproduction data [46–48]. The data are presented assuming $\beta_{\pi N} = 0.485$, $\beta_{\eta N} = 0.46$ (see Sec. VII C). The results of the LF relativistic quark models are given by the dashed [15] and dashed-dotted [17] curves. The solid curves are the central values of the amplitudes found within light-cone sum rules using lattice results for light-cone distribution amplitudes of the $N(1535)S_{11}$ resonance [85].

all channels different from πN and ηN, we find

$$\beta_{\pi N} = 0.485 \pm 0.008 \pm 0.023, \quad (31)$$

$$\beta_{\eta N} = 0.460 \pm 0.008 \pm 0.022. \quad (32)$$

The first error corresponds to the fit error in Eq. (30), and the second error is related to the uncertainty of $\beta_{\pi\pi N}$. The results shown in Fig. 14 correspond to $\beta_{\pi N} = 0.485$, $\beta_{\eta N} = 0.46$.

The CLAS data on π electroproduction allowed the extraction of the longitudinal helicity amplitude for the $\gamma^* N \to N(1535)S_{11}$ transition with good precision. These results are crucial for testing theoretical models. It turned out that at $Q^2 < 2$ GeV^2, the sign of $S_{1/2}$ is not described by the quark models. Here it should be mentioned that quark model predictions for the relative signs between the $S_{1/2}$ and $A_{1/2}$, $A_{3/2}$ amplitudes are presented for the transitions $\gamma^* N \to N(1535)S_{11}$ and $N(1520)D_{13}$ (Figs. 14 and 15) according to the investigation made in Ref. [86]. Combined with the difficulties of quark models to describe the substantial coupling of $N(1535)S_{11}$ to the ηN channel [20] and to strange particles [21,22], the difficulty in the description of the sign of $S_{1/2}$ can be indicative of a large meson-cloud contribution and/or of additional $q\bar{q}$ components in this state [24]. Alternative representations of the $N(1535)S_{11}$ as a meson-baryon molecule have been also discussed [32,34–36].

D. $N(1520)D_{13}$ resonance

The results for the $\gamma^* p \to N(1520)D_{13}$ helicity amplitudes are shown in Fig. 15, where the transverse amplitudes are compared with those extracted from earlier data. The new data provide much more accurate results.

Sensitivity of the earlier data to the $\gamma^* p \to N(1520)D_{13}$ longitudinal helicity amplitude was limited. The CLAS data allowed this amplitude to be determined with good precision and in a wide range of Q^2.

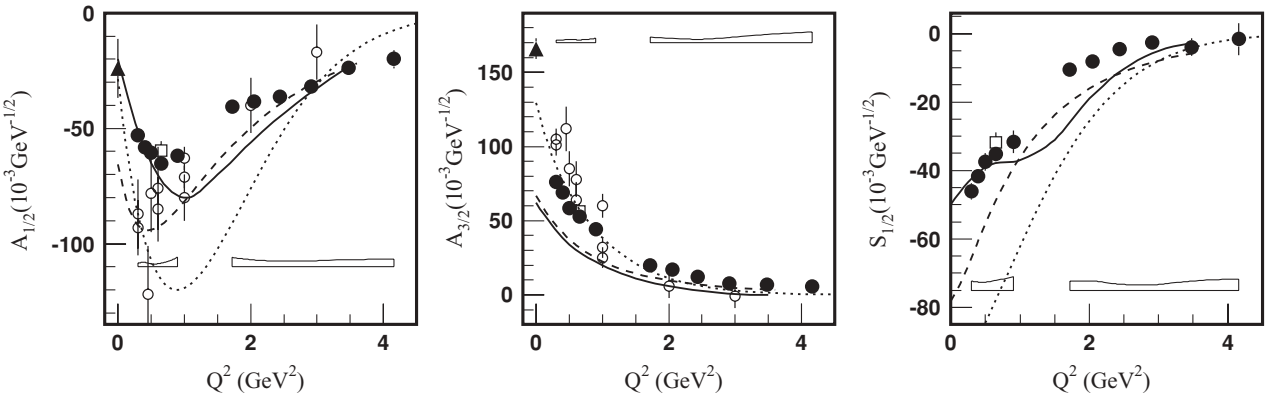

FIG. 15. Helicity amplitudes for the $\gamma^* p \to N(1520)D_{13}$ transition. The legend is partly as for Fig. 13. Open circles show the results [87] extracted from earlier DESY [45,88] and NINA [89] data. The curves correspond to the predictions of the quark models: [90] (solid), [91] (dashed), and [92] (dotted).

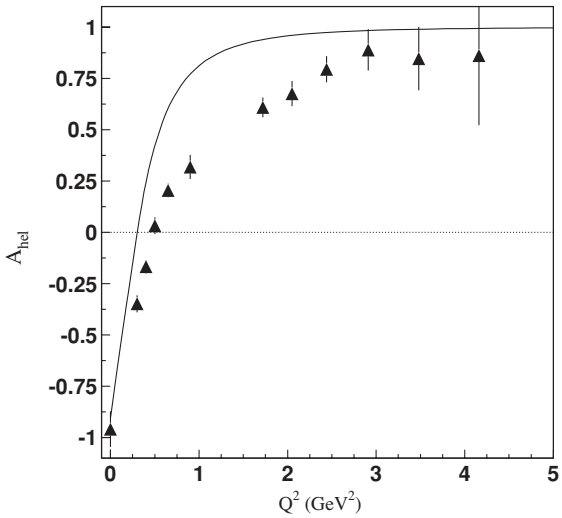

FIG. 16. Helicity asymmetry $A_{\rm hel} \equiv (A_{1/2}^2 - A_{3/2}^2)/(A_{1/2}^2 + A_{3/2}^2)$ for the $\gamma^* p \to N(1520)D_{13}$ transition. Triangles show the results obtained in this work. The solid curve is the prediction of the quark model with the harmonic oscillator potential [93].

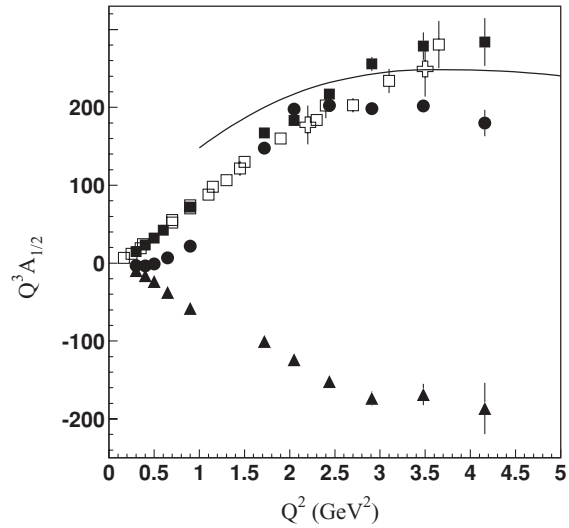

FIG. 17. Helicity amplitudes $A_{1/2}$ for the $\gamma^* p \to N(1440)P_{11}$, $N(1520)D_{13}$, and $N(1535)S_{11}$ transitions, multiplied by Q^3. The results obtained in this work from the JLab-CLAS data on pion electroproduction on the protons are shown by solid circles [$N(1440)P_{11}$], solid triangles [$N(1520)D_{13}$], and solid boxes [$N(1535)S_{11}$]. Open boxes and crosses are the results for the $N(1535)S_{11}$ obtained in η electroproduction, respectively, in HALL B [47,48] and HALL C [46]. The solid curve corresponds to the amplitude $A_{1/2}$ for the $\gamma^* p \to N(1535)S_{11}$ transition found within light-cone sum rules [85].

The obtained results show the rapid helicity switch from the dominance of the $A_{3/2}$ amplitude at the photon point to the dominance of $A_{1/2}$ at $Q^2 > 1$ GeV^2. This is demonstrated in Fig. 16 in terms of the helicity asymmetry. Such behavior was predicted by a nonrelativistic quark model with harmonic oscillator potential [94]. Quark models also describe the sign and Q^2 dependence of the longitudinal amplitude. However, there are some shortcomings in the quark model description of the details of the Q^2 dependence of the $\gamma^* p \to N(1520)D_{13}$ amplitudes. The amplitude $A_{3/2}$ is significantly underestimated in all quark models for $Q^2 < 2$ GeV^2. Dynamical models predict large meson-cloud contributions to this amplitude [83] that could explain the discrepancy.

Finally, Fig. 17 shows the helicity amplitudes $A_{1/2}$ for the resonances $N(1440)P_{11}$, $N(1520)D_{13}$, and $N(1535)S_{11}$, multiplied by Q^3. The data indicate that starting with $Q^2 = 3$ GeV^2, these amplitudes have a Q^2 dependence close to $1/Q^3$. Such behavior is expected in pQCD in the limit $Q^2 \to \infty$ [95]. Measurements at higher Q^2 are needed in order to check a possible Q^3 scaling of these amplitudes.

VIII. SUMMARY

The electroexcitation amplitudes for the low-mass resonances $\Delta(1232)P_{33}$, $N(1440)P_{11}$, $N(1520)D_{13}$, and $N(1535)S_{11}$ are determined in a wide range of Q^2 in the comprehensive analysis of JLab-CLAS data on differential cross sections, longitudinally polarized beam asymmetries, and longitudinal target and beam-target asymmetries for π electroproduction off the proton. A total of about 119 000 data points were included covering the full azimuthal and polar angle range. With this, we have complemented the previous analyses [41,42,82] by including all JLab-CLAS pion electroproduction data available today. We also have put significant effort into accounting for model and systematic uncertainties of the extracted electroexcitation amplitudes by including the uncertainties of hadronic parameters, such as the masses and widths of the resonances, the amplitudes of higher lying resonances, the parameters that determine nonresonant contributions, as well as the point-to-point systematics of the experimental data and the overall normalization error of the cross sections. Utilization of two approaches, DR and UIM, allowed us to also estimate the model dependence of the results, which was taken into account in the total model uncertainties of the extracted amplitudes.

There are still additional uncertainties in the amplitudes presented in this paper. These are related to the lack of precise knowledge of the empirical resonance couplings to the $N\pi$ channel. However, we did not include these uncertainties in the error budget as this is an overall multiplicative correction that affects all amplitudes for a given resonance equally, and, more importantly, the amplitudes can be corrected for these effects once improved hadronic couplings become available.

The amplitudes for the electroexcitation of the $\Delta(1232)P_{33}$ resonance are determined in the range $0.16 \leqslant Q^2 \leqslant 6$ GeV^2. The results are in agreement with the low-Q^2 data from MAMI [75,76] and MIT Bates [77] and with data from the JLab Hall A ($Q^2 = 1$ GeV^2) [79,80] and Hall C ($Q^2 = 2.8, 4.2$ GeV^2) [78].

The results for the $\Delta(1232)P_{33}$ resonance show the importance of the meson-cloud contribution to quantitatively explain the magnetic dipole strength, as well as the electric and scalar quadrupole transitions. They also do not show any tendency of approaching the asymptotic QCD regime for $Q^2 \leqslant 6$ GeV^2.

This was already mentioned in the original paper [5], where the analysis was based on the UIM approach only.

The amplitudes for the electroexcitation of the resonances $N(1440)P_{11}$, $N(1520)D_{13}$, and $N(1535)S_{11}$ are determined in the range $0.3 \leqslant Q^2 < 4.5\ \mathrm{GeV}^2$.

For the Roper resonance, the high-Q^2 amplitudes ($Q^2 =$ 1.7–4.5 GeV^2) and the results for $Q^2 = 0.4$ and $0.65\,\mathrm{GeV}^2$ were already presented and discussed in Refs. [41,82]. In the present paper, the data for $Q^2 = 0.4$ and $0.65\,\mathrm{GeV}^2$ were reanalyzed taking into account the recent CLAS polarization measurements on the target and beam-target asymmetries [8]. Also included are the new results at $Q^2 = 0.3$, 0.525, and $0.9\,\mathrm{GeV}^2$. The main conclusion for the Roper resonance is, as already reported in Ref. [82], that the data on $\gamma^* p \to N(1440)P_{11}$ available in the wide range of Q^2 provide strong evidence that this state is predominantly the first radial excitation of the three-quark ground state.

For the first time, the $\gamma^* p \to N(1535)S_{11}$ transverse helicity amplitude has been extracted from the π electroproduction data up to $Q^2 = 4.5\ \mathrm{GeV}^2$. The results confirm the Q^2 dependence of this amplitude as observed in η electroproduction. The transverse amplitude found from the π and η data allowed us to specify the branching ratios to the πN and ηN channels for the $N(1535)S_{11}$.

Thanks to the CLAS measurements of π electroproduction, the $\gamma^* p \to N(1520)D_{13}$ and $N(1535)S_{11}$ longitudinal helicity amplitudes have been determined for the first time from experimental data. For the $\gamma^* p \to N(1535)S_{11}$ transition, the sign of $S_{1/2}$ is not described by quark models at $Q^2 < 2\ \mathrm{GeV}^2$. Combined with the difficulties of quark models in describing the substantial coupling of the $N(1535)S_{11}$ to the ηN and strangeness channels, this can be an indication of a large meson-cloud contribution and/or of additional $q\bar{q}$ components in this state; alternative representations of the $N(1535)S_{11}$ as a meson-baryon molecule are also possible.

The CLAS data provide much more accurate results for the $\gamma^* p \to N(1520)D_{13}$ transverse helicity amplitudes than those extracted from earlier DESY and NINA data. The data confirm the constituent quark model prediction of the rapid helicity switch from the dominance of the $A_{3/2}$ amplitude at the photon point to the dominance of $A_{1/2}$ at $Q^2 > 1\ \mathrm{GeV}^2$. Quark models also describe the sign and Q^2 dependence of the longitudinal amplitude.

Starting with $Q^2 = 3\ \mathrm{GeV}^2$, the helicity amplitudes $A_{1/2}$ for the resonances $N(1440)P_{11}$, $N(1520)D_{13}$, and $N(1535)S_{11}$ have a behavior close to $1/Q^3$. Measurements at higher Q^2 are needed in order to check Q^3 scaling for these amplitudes.

ACKNOWLEDGMENTS

This work was supported in part by the US Department of Energy and the National Science Foundation, the Korea Research Foundation, the French Commissariat a l'Energie Atomique and CNRS/IN2P3, the Italian Istituto Nazionale di Fisica Nucleare, the Skobeltsyn Institute of Nuclear Physics and Physics Department at Moscow State University, and the UK Science and Technology Facilities Research Council (STFC). Jefferson Science Associates, LLC, operates Jefferson Lab under US DOE Contract No. DE-AC05-060R23177.

[1] K. Joo *et al.* (CLAS Collaboration), Phys. Rev. Lett. **88**, 122001 (2002).
[2] K. Joo *et al.* (CLAS Collaboration), Phys. Rev. C **68**, 032201 (2003).
[3] K. Joo *et al.* (CLAS Collaboration), Phys. Rev. C **70**, 042201 (2004).
[4] H. Egiyan *et al.* (CLAS Collaboration), Phys. Rev. C **73**, 025204 (2006).
[5] M. Ungaro *et al.* (CLAS Collaboration), Phys. Rev. Lett. **97**, 112003 (2006).
[6] L. C. Smith *et al.* (CLAS Collaboration), AIP Conf. Proc. **904**, 232 (2007).
[7] K. Park *et al.* (CLAS Collaboration), Phys. Rev. C **77**, 015208 (2008).
[8] A. Biselli *et al.* (CLAS Collaboration), Phys. Rev. C **78**, 045204 (2008).
[9] S. D. Drell and T. M. Yan, Phys. Rev. Lett. **24**, 181 (1970).
[10] V. B. Berestetskii and M. V. Terent'ev, Sov. J. Nucl. Phys. **24**, 547 (1976); **25**, 347 (1977).
[11] S. J. Brodsky and S. D. Drell, Phys. Rev. D **22**, 2236 (1980).
[12] I. G. Aznauryan, A. S. Bagdasaryan, and N. L. Ter Isaakyan, Phys. Lett. **B112**, 393 (1982); Yad. Fiz. **36**, 1278 (1982).
[13] I. G. Aznauryan and A. S. Bagdasaryan, Yad. Fiz. **41**, 249 (1985).
[14] H. J. Weber, Phys. Rev. C **41**, 2783 (1990).
[15] S. Capstick and B. D. Keister, Phys. Rev. D **51**, 3598 (1995).
[16] F. Cardarelli, E. Pace, G. Salmé, and S. Simula, Phys. Lett. **B357**, 267 (1995).
[17] E. Pace, G. Salmé, and S. Simula, Few-Body Syst. Suppl. **10**, 407 (1999); E. Pace, G. Salmé, F. Cardarelli, and S. Simula, Nucl. Phys. **A666**, 33 (2000).
[18] B. Juliá-Díaz, D. O. Riska, and F. Coester, Phys. Rev. C **69**, 035212 (2004).
[19] I. G. Aznauryan, Phys. Rev. C **76**, 025212 (2007).
[20] C. Amsler *et al.* (Particle Data Group), Phys. Lett. **B667**, 1 (2008).
[21] B. C. Liu and B. S. Zou, Phys. Rev. Lett. **96**, 042002 (2006).
[22] J. J. Xie, B. S. Zou, and H. C. Chiang, Phys. Rev. C **77**, 015206 (2008).
[23] Q. B. Li and D. O. Riska, Phys. Rev. C **74**, 015202 (2006).
[24] C. S. An and B. S. Zou, arXiv:0802.3996 [nucl-th].
[25] S. S. Kamalov and S. N. Yang, Phys. Rev. Lett. **83**, 4494 (1999).
[26] S. S. Kamalov, S. N. Yang, D. Drechsel, O. Hanstein, and L. Tiator, Phys. Rev. C **64**, 032201(R) (2001).
[27] T. Sato and T.-S. H. Lee, Phys. Rev. C **63**, 055201 (2001).
[28] A. Matsuyama, T. Sato, and T.-S. H. Lee, Phys. Rep. **439**, 193 (2007).
[29] C. Alexandrou, G. Koutsou, H. Neff, J. W. Negele, W. Schroers, and A. Tsapalis, Phys. Rev. D **77**, 085012 (2008).
[30] Z. P. Li, Phys. Rev. D **44**, 2841 (1991).
[31] Z. P. Li, V. Burkert, and Zh. Li, Phys. Rev. D **46**, 70 (1992).
[32] N. Kaiser, P. B. Siegel, and W. Weise, Phys. Lett. **B362**, 23 (1995).

[33] O. Krehl, C. Hanhart, C. Krewald, and J. Speth, Phys. Rev. C **62**, 025207 (2000).
[34] J. Nieves and E. R. Arriola, Phys. Rev. D **64**, 116008 (2001).
[35] T. Inoue, E. Oset, and M. J. Vicente Vacas, Phys. Rev. C **65**, 035204 (2002).
[36] E. E. Kolomeitsev and M. F. M. Lutz, Phys. Lett. **B585**, 243 (2004).
[37] V. Pascalutsa, M. Vanderhaeghen, and S. N. Yang, Phys. Rep. **437**, 125 (2007).
[38] M. V. Polyakov and K. M. Semenov-Tian-Shansky, Eur. Phys. J. A **40**, 181 (2009).
[39] D. Drechsel, S. Kamalov, and L. Tiator, Eur. Phys. J. A **34**, 69 (2007).
[40] I. G. Aznauryan, Phys. Rev. C **67**, 015209 (2003).
[41] I. G. Aznauryan, V. D. Burkert, H. Egiyan, K. Joo, R. Minehart, and L. C. Smith, Phys. Rev. C **71**, 015201 (2005).
[42] I. G. Aznauryan, V. D. Burkert, G. V. Fedotov, B. S. Ishkhanov, and V. I. Mokeev, Phys. Rev. C **72**, 045201 (2005).
[43] J. C. Alder *et al.*, Nucl. Phys. **B99**, 1 (1975).
[44] G. V. Fedotov *et al.* (CLAS Collaboration), Phys. Rev. C **79**, 015204 (2009).
[45] R. Haidan, DESY-F21-79/03 (unpublished).
[46] C. S. Armstrong *et al.*, Phys. Rev. D **60**, 052004 (1999).
[47] R. Thompson *et al.* (CLAS Collaboration), Phys. Rev. Lett. **86**, 1702 (2001).
[48] H. Denizli *et al.* (CLAS Collaboration), Phys. Rev. C **76**, 015204 (2007).
[49] R. C. E. Devenish and D. H. Lyth, Phys. Rev. D **5**, 47 (1972).
[50] D. Drechsel, O. Hanstein, S. Kamalov, and L. Tiator, Nucl. Phys. **A645**, 145 (1999).
[51] R. A. Arndt, I. I. Strakovsky, and R. L. Workman, Phys. Rev. C **53**, 430 (1996).
[52] R. A. Arndt, W. J. Briscoe, I. I. Strakovsky, and R. L. Workman, Phys. Rev. C **66**, 055213 (2002).
[53] R. L. Walker, Phys. Rev. **182**, 1729 (1969).
[54] M. Guidal, J.-M. Laget, and M. Vanderhaeghen, Nucl. Phys. **A627**, 645 (1997).
[55] M. Guidal, J.-M. Laget, and M. Vanderhaeghen, Phys. Lett. **B400**, 6 (1997).
[56] M. Vanderhaeghen, M. Guidal, and J.-M. Laget, Phys. Rev. C **57**, 1454 (1998).
[57] J. Arrington, W. Melnitchouk, and J. A. Tjon, Phys. Rev. C **76**, 035205 (2007).
[58] A. Lung *et al.*, Phys. Rev. Lett. **70**, 718 (1993).
[59] J. Lachniet *et al.* (CLAS Collaboration), Phys. Rev. Lett. **102**, 192001 (2009).
[60] C. J. Bebek *et al.*, Phys. Rev. D **13**, 25 (1976).
[61] C. J. Bebek *et al.*, Phys. Rev. D **17**, 1693 (1978).
[62] T. Horn *et al.*, Phys. Rev. Lett. **97**, 192001 (2006).
[63] V. Tadevosyan *et al.*, Phys. Rev. C **75**, 055205 (2007).
[64] R. Madey *et al.*, Phys. Rev. Lett. **91**, 122002 (2003).
[65] V. Eletski and Ya. Kogan, Yad. Fiz. **39**, 138 (1984).
[66] I. Aznauryan and K. Oganessyan, Phys. Lett. **B249**, 309 (1990).
[67] R. A. Arndt, W. J. Briscoe, I. I. Strakovsky, R. L. Workman, and M. M. Pavan, Phys. Rev. C **69**, 035213 (2004).
[68] R. A. Arndt, W. J. Briscoe, I. I. Strakovsky, and R. L. Workman, Phys. Rev. C **74**, 045205 (2006).
[69] R. A. Arndt, R. L. Workman, Zh. Li, and L. D. Roper, Phys. Rev. C **42**, 1864 (1990).
[70] L. Tiator, D. Drechsel, S. Kamalov, and S. N. Yang, PiN Newslett. **16**, 41 (2002).
[71] V. D. Burkert, R. DeVita, M. Battaglieri, M. Ripani, and V. Mokeev, Phys. Rev. C **67**, 035204 (2003).
[72] D. Drechsel and L. Tiator, J. Phys. G **18**, 449 (1992).
[73] W. W. Ash, Phys. Lett. **B24**, 165 (1967).
[74] H. F. Jones and M. D. Scadron, Ann. Phys. (NY) **81**, 1 (1973).
[75] S. Stave *et al.*, Eur. Phys. J. A **30**, 471 (2006).
[76] N. F. Sparveris *et al.*, Phys. Lett. **B651**, 102 (2007).
[77] N. F. Sparveris *et al.*, Phys. Rev. Lett. **94**, 022003 (2005).
[78] V. V. Frolov *et al.*, Phys. Rev. Lett. **82**, 45 (1999).
[79] J. J. Kelly *et al.*, Phys. Rev. Lett. **95**, 102001 (2005).
[80] J. J. Kelly *et al.*, Phys. Rev. C **75**, 025201 (2007).
[81] V. Pascalutsa and M. Vanderhaeghen, Phys. Rev. D **76**, 111501(R) (2007).
[82] I. G. Aznauryan *et al.* (CLAS Collaboration), Phys. Rev. C **78**, 045209 (2008).
[83] B. Juliá-Díaz, T.-S. H. Lee, A. Matsuyama, T. Sato, and L. C. Smith, Phys. Rev. C **77**, 045205 (2008).
[84] I. G. Aznauryan, Phys. Rev. C **68**, 065204 (2003).
[85] V. M. Braun *et al.*, Phys. Rev. Lett. **103**, 072001 (2009).
[86] I. G. Aznauryan, V. D. Burkert, and T.-S. H. Lee, arXiv:0810.0997 [nucl-th].
[87] F. Foster and G. Hughes, Rep. Prog. Phys. **46**, 1445 (1983).
[88] J. C. Alder *et al.*, Nucl. Phys. **B91**, 386 (1975); **B105**, 253 (1976).
[89] W. J. Shuttleworth *et al.*, Nucl. Phys. **B45**, 428 (1972); E. Evangelides *et al.*, *ibid.* **B71**, 381 (1974); A. Latham *et al.*, *ibid.* **B156**, 58 (1979); J. Wright *et al.*, *ibid.* **B181**, 403 (1981); A. Latham *et al.*, *ibid.* **B189**, 1 (1981).
[90] M. Warns, H. Schröder, W. Pfeil, and H. Rollnik, Z. Phys. C **45**, 627 (1990).
[91] M. Aiello, M. M. Giannini, and Santopinto, J. Phys. G **24**, 753 (1998).
[92] D. Merten, U. Löring, K. Kretzschmar, B. Metsch, and H.-R. Petry, Eur. Phys. J. A **14**, 477 (2002).
[93] R. Koniuk and N. Isgur, Phys. Rev. D **21**, 1868 (1980).
[94] F. E. Close and F. J. Gilman, Phys. Lett. **B38**, 541 (1972).
[95] C. E. Carlson, Phys. Rev. D **34**, 2704 (1986); C. E. Carlson and J. L. Poor, *ibid.* **38**, 2758 (1988).